Colocalized, Bidirectional Optogenetic Modulations in Freely Behaving Mice with a Wireless Dual-Color Optoelectronic Probe

Lizhu Li,[1, #] Lihui Lu,[2, 3, #] Yuqi Ren,[2, 3, #] Guo Tang,[1, #] Yu Zhao,[1] Xue Cai,[1] Zhao Shi,[1] He Ding,[4] Changbo Liu,[5] Dali Cheng,[1] Yang Xie,[1] Huachun Wang,[1] Xin Fu,[6] Lan Yin,[6] Minmin Luo,[2, 3, 7, *] Xing Sheng [1, 7, *]

Affiliations

[1]Department of Electronic Engineering, Beijing National Research Center for Information Science and Technology, Center for Flexible Electronics Technology, Tsinghua University, Beijing, China

[2]Chinese Institute for Brain Research, Beijing, China

[3]National Institute of Biological Sciences and School of Life Sciences, Tsinghua University, Beijing, China

[4]Beijing Engineering Research Center of Mixed Reality and Advanced Display, School of Optics and Photonics, Beijing Institute of Technology, Beijing, China

[5]School of Materials Science and Engineering and Hangzhou Innovation Institute, Beihang University, Beijing, China

[6]School of Materials Science and Engineering, Tsinghua University, Beijing, China

[7]IDG/McGovern Institute for Brain Research, Tsinghua University, Beijing, China

# L. Li, L. Lu, Y. R., and G. T. contributed equally to this work.

*Correspondence to: luominmin@cibr.ac.cn; xingsheng@tsinghua.edu.cn

ABSTRACT

The precise control of neural activities at both cellular and circuit levels reveals significant impacts on the fundamental neuroscience explorations and medical applications. Optogenetic methods provide efficient cell-specific modulations, and the ability of simultaneous neural activation and inhibition in the same brain region of freely moving animals is highly desirable and being actively researched. Here we report bidirectional neuronal activity manipulation accomplished by a wireless, dual-color optogenetic probe in synergy with the co-expression of two spectrally distinct opsins (ChrimsonR and stGtACR2) in a rodent model. Based on vertically assembled, thin-film microscale light-emitting diodes (micro-LEDs) with a lateral dimension of 125 × 180 μm^2 on flexible substrates, the dual-color probe shows colocalized red and blue emissions and allows chronic *in vivo* operations with desirable biocompatibilities. In addition, we discover that neurons co-expressing the two opsins can be deterministically evoked or silenced under red or blue irradiations. Implanted in behaving mice, the wirelessly controlled dual-color probe interferes with dopaminergic neurons in the ventral tegmental area (VTA), increasing or decreasing dopamine levels with colocalized red and blue stimulations. Such bidirectional regulations further generate rewarding and aversive behaviors of freely moving mice in a place preference test and interrogate social interactions among multiple mice. The technologies established here will create numerous opportunities and profound implications for brain research.

INTRODUCTION

Understanding brain functions and treating neurological disorders rely on the continuous development of advanced technologies to interrogate complex nervous systems[1, 2]. Over the past decades, optogenetic methods have been emerging as a powerful toolset for effective and precise neural manipulation, owing to their capability of specific cell targeting[3, 4]. Until now, a range of genetically encoded, light-sensitive proteins (opsins) with distinct spectral responses have been engineered to regulate flows of different cations and anions[5, 6, 7, 8, 9, 10, 11, 12, 13, 14, 15], triggering various biological responses, from cells and *C. elegans* to rodents and non-human primates[16, 17, 18, 19]. Accompanying the development of opsins, advanced technologies for light delivery into the brain have also been progressing rapidly. Apart from various waveguide-based emitters interfacing with external light sources[20, 21, 22], recently developed implantable probes based on thin-film, microscale optoelectronic devices have offered a viable solution to versatile neural modulations in untethered animals, when incorporated with various wirelessly operating systems based on radio frequency (RF) antennas[23, 24, 25], near-field communication (NFC)[26], Bluetooth chips[27], and infrared receivers[28]. In addition to these achievements, bidirectional neural modulations, specifically, by activating or suppressing the same or different populations of cells in behaving animals with the light of different wavelengths, are highly demanded. Such capabilities would enable more precise control of neural activities to advance both neuroscience explorations and disease medications[29]. Certain efforts have been attempted, including explorations based on experiments by expressing excitatory and inhibitory opsins in separate animals[30, 31] or distinct cells in different neural regions[17, 32]. There are also reports on dual-color optogenetic activation and inhibition by co-expressing different opsins in the same cells[33, 34, 35, 36]. Recent efforts also remarkably demonstrate bidirectional optogenetic modulations with implantable waveguides coupled to extra-cranial dual-color laser sources and their combination with *in*

67 *vivo* electrophysiological recordings[23, 36, 37], but the wireless operation has not been achieved.
68 Therefore, we envision that wirelessly operated light sources with polychromatic emissions,
69 which collaborate with co-expressed opsins, can be implemented for untethered use in freely
70 moving animals and enable previously inaccessible applications.

71 This study presents synergic optoelectronic and biological strategies to overcome
72 challenges of existing techniques, and realize colocalized, bidirectional neural manipulations
73 in untethered behaving mice. With heterogeneously integrated thin-film, microscale light-
74 emitting diodes (micro-LEDs), a wirelessly operated, implantable dual-color probe allows
75 independently controlled red and blue emissions in the same region. We also discover that the
76 co-expression of two channelrhodopsins (ChrimsonR and stGtACR2) in the same group of
77 neurons enables efficient light-evoked cell depolarization and hyperpolarization with
78 controlled cation and anion flows under red and blue illuminations, respectively. With the
79 wireless, dual-color micro-LED probes implanted into the ventral tegmental area (VTA) of
80 freely moving mice, preference and aversion tests of individual and social behaviors clearly
81 demonstrate the bidirectional optogenetic excitation and inhibition capability. Furthermore, *in*
82 *vivo* behavioral results associated with the red and blue stimulations in the VTA are validated
83 by increased or decreased dopamine levels detected in the nucleus accumbens (NAc) in real-
84 time.

85

86 **RESULTS**

87 **Wirelessly operated, dual-color micro-LED probes and circuit systems**

88 We design and implement a wireless, dual-color micro-LED probe that generates red
89 and blue emissions in the same brain region for bidirectional optogenetic modulations *in vivo*,
90 as schematically illustrated in Figure 1a. Our previous works establish wirelessly operated
91 microscale optoelectronic device strategy for *in vivo*, single-color optogenetic stimulations[37,

92 [38, 39, 40], here these concepts are applied for dual-color, bidirectional modulations. Specifically,
93 with the co-expression of spectrally distinct ion channels, ChrimsonR[7] and stGtACR2[9], in the
94 same population of cells, red and blue light regulates the inflow of cations and anions,
95 causing cell depolarization and hyperpolarization, respectively (Figure 1b). Figure 1c
96 displays an enlarged view of the dual-color probe, with design and fabrication details
97 provided in the Methods and Figure S1. From bottom to top, the probe structure comprises of
98 a copper (Cu) coated polyimide (PI) thin-film substrate, an indium gallium phosphide (InGaP)
99 red LED, a silicon oxide (SiO_2) / titanium oxide (TiO_2) based dielectric filter, and an indium
100 gallium nitride (InGaN) blue LED. The Cu coating on PI serves as an efficient heat spreader
101 to reduce the probe's operation temperature[37]. All the devices (red LEDs, blue LEDs, and
102 filters) are formed in thin-film, microscale formats (lateral dimension ~ 125 μm × 180 μm,
103 thickness ~ 5–7 μm) through epitaxial liftoff, and vertically assembled via transfer printing[37,
104 39, 40] (Figure 1d). The dimensions of our LEDs are designed to target a large nucleus like
105 VTA. Although smaller devices down to 10–20 μm can be fabricated[41, 42], reducing LED size
106 decreases luminescence efficiencies[43, 44] and may cause additional tissue heating. The
107 intrinsic optical transparency of active layers in the InGaN blue micro-LED allows emissions
108 from the red micro-LED to pass through with minimal losses. Additionally, the designed
109 filter selectively reflects blue light and transmits red light, enhancing the emissive
110 efficiencies of both micro-LEDs.

111 Flexible PI substrates with vertically stacked micro-LEDs are laser milled and
112 encapsulated with a waterproof coating, forming a needle-shaped probe with a dimension
113 (thickness ~120 μm and width ~320 μm) similar to a conventional silica fiber (diameter ~220
114 μm) used in optogenetic stimulations. The Cu coated PI substrate has a measured Young's
115 modulus of ~15 GPa, softer than silicon (~180 GPa) and tungsten (~400 GPa), but still much
116 harder than the brain tissue (~1 kPa). The formed probe has a bending stiffness of ~9×10^4

117 pNm^2, similar to metal electrodes used for electrophysiological studies[45]. Separate
118 metallization and electrical insulation ensure that red and blue micro-LEDs can be
119 independently lighted up and display spectrally varied illuminations (red, blue, or combined)
120 in the same location (Figure 1e and Movie S1). Figure 1f plots measured electroluminescence
121 (EL) spectra. The red and blue micro-LEDs exhibit emission peaks at 630 nm and 480 nm,
122 which are in good accordance with the excitation spectra of ChrimsonR and stGtACR2 (data
123 extracted from references[7, 8]), respectively. Moreover, the spectral separation between the two
124 opsins, guarantee precise optogenetic activation and inhibition with minimal optical
125 interferences. More optoelectronic properties of the dual-color micro-LED probe, including
126 current-voltage characteristics, quantum efficiencies, power irradiance, and angular-
127 dependent emissive profiles are presented in Figure S2. Under injection currents of 10 mA,
128 the red and the blue micro-LEDs can reach irradiances up to 50 mW/mm^2 and 200 mW/mm^2
129 on the device surface, which are sufficient for optogenetic modulations. In addition, both
130 devices exhibit a uniform, near Lambertian emission profile.

131 To illustrate the optical performance of the devices, we insert a dual-color probe into
132 a brain phantom (Figure 1g, top). For comparison, established models calculate optical
133 profiles based on the optical properties (absorption and scattering) of brain tissues (Figure 1g,
134 bottom). Both experimental and simulation results reveal that vertically stacked dual-color
135 micro-LEDs show colocalized red and blue emission profiles, ensuring effective activation
136 and inhibition in the same brain region. Power irradiances for blue and red emissions
137 decrease to 10% of the original power at propagating distances of ~400 μm and ~800 μm,
138 respectively. Compared to a probe with laterally arranged red and blue micro-LEDs
139 displaying misaligned emissions with a relatively small overlapping volume of light, the
140 vertically assembled device provides a smaller footprint and generates an optimal
141 overlapping profile for dual-color stimulations.

142 Thermal behaviors of the micro-LED probe are also systematically analyzed, with
143 detailed results presented in Figures S3 and S4. Probes are inserted into the brain phantom as
144 well as the living mouse brain, with temperature rises measured by an infrared camera and a
145 thermocouple. Both experiments obtain similar results and are in agreement with the thermal
146 models established based on finite-element analysis. Under a pulsed operation (20-Hz
147 frequency, 10-ms pulse duration, current 0–10 mA), the tissue temperature rises caused by
148 the red micro-LED can be restricted within 1 °C. The operation of the blue micro-LED
149 induces a higher thermal effect because practical neural inhibition for stGtACR2 requires
150 continuous current injection; nonetheless, the tissue heating can be controlled within 2 °C by
151 limiting the current within 5 mA. Such operation modes for red and blue micro-LEDs will be
152 employed throughout *in vivo* experiments, to mitigate undesired neural responses and
153 possible tissue damage due to overheating.

154 We also design a customized, miniaturized flexible circuit module to wirelessly
155 operate the dual-color micro-LED probe. Compared to previous reports[22, 36] on tethered fiber
156 or laser coupled devices for dual-color stimulations, the wireless operation here enables the
157 study of complex behaviors of freely moving animals more conveniently. Controlled by radio
158 frequency (RF) communication at 2.4 GHz, the battery-powered circuit (weight ~1.9 g)
159 independently addresses the red and the blue micro-LEDs, by adjusting their pulse
160 frequencies, durations, and injection currents for versatile neural modulations *in vivo* (Figure
161 1h, and details in the Methods and Figures S5–S9). Designed programming commands also
162 allow the independent operation of multiple micro-LED probes in synchronized or non-
163 synchronized modes (Movie S2). After subcranial implanting the micro-LED probe into a
164 behaving mouse, the light-weighted circuit mounted onto the mouse head provides the
165 capability for optogenetic control in an untethered manner (Figure 1i).

166

167 **Bidirectional optogenetic manipulations of neurons *in vitro*, with dual-color stimulations**

168 We first evaluate the feasibility of dual-color, bidirectional optogenetic modulations for
169 neurons co-expressing ChrimsonR and stGtACR2 in brain slices with electrophysiological
170 tests. Mixed vectors of AAV-CAG-DIO-ChrimsonR-mCherry and AAV-EF1a-DIO-
171 stGtACR2-EGFP are injected into the ventral tegmental area (VTA) of *DAT-Cre* mice
172 (Figure 2a). The deployment of the soma-targeted variant stGtACR2 exhibits performance
173 superior to previously reported anion channel GtACR2, by enhancing the membrane
174 trafficking and reducing the axonal excitation[8, 9]. Figure 2b shows the fluorescence images of
175 stained cells 3 weeks after viral injection in the VTA, including 4',6-diamidino-2-
176 phenylindole (DAPI, blue), stGtACR2 (green), and ChrimsonR (red). The merged graph and
177 zoomed-in views (Figure 2c) clearly reveal the desirable co-expression of the two opsins in
178 target cells. Statistical results show that ~30% of cells are labeled with stGtACR2 or
179 ChrimsonR, and about 83% of these labeled cells co-express both opsins on average (Figure
180 2d).

181 Whole-cell patch recordings capture intracellular signals of these cells under optical
182 stimulations (Figure 2e). Other than using our designed micro-LED probe, here we employ a
183 collimated light spot with coupled red (633 nm) and blue (480 nm) laser sources for *in vitro*
184 experiments, to achieve uniform illuminations for better power calibrations. Figures 2f and 2g
185 validate that pulsed red stimulations (20-Hz frequency, 10-ms pulse duration) induce action
186 potentials (APs or spikes) by depolarizing these cells, and spike activation probability
187 increases at elevated red irradiances. In these same cells, continuous blue stimulations
188 suppress activities by hyperpolarization (Figures 2h–2j). Voltage clamp results illustrate that
189 blue light evokes photocurrent reversion when the membrane potential becomes more
190 positive (Figure 2h), and the probability for spike inhibition also increases at elevated blue
191 irradiances (Figures 2i and 2j). Threshold irradiances for complete spike activation and

192 inhibition are around 10 mW/mm^2 and 1 mW/mm^2 for red and blue illuminations,
193 respectively. The results are consistent with previous reports on cells expressing only
194 ChrimsonR or stGtACR2[7, 9].

195 Notably, we do not only demonstrate that the co-expression of both opsins does not
196 affect the efficacy of cell activity excitation or suppression, but also accomplish bidirectional
197 activation and inhibition in the same cell by instantaneously altered red and blue irradiations
198 (Figure 2k). In accordance with the activation spectra of two opsins (Figure 1f), red light does
199 not interact with stGtACR2, which exhibits nearly zero responses at wavelengths longer than
200 600 nm. On the other hand, ChrimsonR should have responded to blue light, which could
201 raise a concern about possible optical crosstalk. Nevertheless, spike activations caused by
202 blue light do not occur in cells co-expressing ChrimsonR and stGtACR2, since cells are
203 suppressed by turning on stGtACR2 channels at a much lower blue irradiance. This fact can
204 be confirmed by patching the cells under combined red and blue illuminations (Figures 2l and
205 2m). Example traces in Figure 2l show that red-light-evoked spikes are suppressed under
206 simultaneous blue illuminations even with very low irradiances. More traces are reported in
207 Figure S10, and Figure 2m summarizes the spike probability (measured and averaged among
208 n = 5 cells) with combined red and blue illuminations. Introducing blue irradiances orders of
209 magnitude lower than red irradiances can effectively suppress cell spikes and cause activity
210 inhibition.

211

212 **Bidirectional optogenetic modulation and simultaneous electrophysiological recording**
213 ***in vivo***

214 Neural activities associated with dual-color stimulations are further examined with
215 simultaneous electrophysiological recordings *in vivo* (Figure S11). Two opsins (ChrimsonR

216 and stGtACR2) are co-expressed in the primary somatosensory cortex of *CaMKII-Cre* mice
217 (Figure S11a). Followed by two weeks of recovery and viral expression, extracellular
218 electrodes, and dual-color micro-LED probes are inserted in the head-fixed mice, with a
219 separation of ~500 μm (Figure S11b). Spontaneous and red-light stimulated waveforms are
220 recorded and sorted, showing typical extracellular spike events (Figure S11c). Multiple trials
221 collected for a sample unit indicate that cell spike rates can be enhanced or decreased by
222 applying red or blue illuminations (Figures S11d and S11e). Results summarized for multiple
223 cells show that the basal spike firing rate (13 Hz) increases to 28 Hz during red illumination
224 and decreases to 2 Hz during blue illumination (Figures S11f and S11g). These results
225 showcase the capability for *in vivo* bidirectional modulations and are in good accordance with
226 the previous report based on a different opsin combination (ChR2 and Jaws)[36].

227

228 **Bidirectional optogenetic modulation of preference and aversion behaviors *in vivo*, with**
229 **wireless dual-color micro-LED probes**

230 Activities of the dopaminergic neurons in the VTA we manage to manipulate in Figure 2
231 significantly correlate with the reward and aversion-based behaviors[46, 47, 48]. In Figure 3, we
232 further exploit the capability of bidirectional optogenetic manipulations by implanting dual-
233 color micro-LED probes into behaving mice. After the injection of AAV-CAG-DIO-
234 ChrimsonR-mCherry and AAV-EF1a-DIO-stGtACR2-EGFP vectors, the dual-color micro-
235 LED probe is implanted into the VTA of *DAT-cre* mice via standard stereotaxic surgery
236 (Figure 3a and Figure S12). Figure 3b presents fluorescence images of a brain slice with a
237 micro-LED probe underneath it, showing the co-expression of ChrimsonR and stGtACR2 in
238 the VTA, combined with the luminescence of the red and the blue micro-LEDs under
239 corresponding optical excitations. To assess the devices' biocompatibility *in vivo*, histological
240 examinations of brain slices show that inflammatory reactions of the micro-LED probe are

241 similar to a conventional silica fiber (diameter ~220 μm) 1 day or 3 weeks' post-implantation
242 (Figure S13), owing to its thin-film geometry, mechanical flexibility, and bio-friendly
243 encapsulation. Also, mass spectrometric analysis shows that the brain tissue has a minimal
244 accumulation of dissolved Cu element 5 weeks' post-implantation (Figure S14). In addition,
245 we perform dynamic calcium imaging on acute brain slices for AAV-hsyn-GCaMP6m
246 expressing mice 2 weeks' post-implantation (Figure S15). Cell activities can be effectively
247 recorded in neurons ~100 μm away from the lesion region, in agreement with the histological
248 analysis. Moreover, the parylene-based, waterproof encapsulation maintains the micro-LEDs'
249 chronic and stable operation for more than 200 days after implantation (Figure S16).

250 *In vivo* experiments are performed within a real-time place preference/avoidance
251 (RTPP) paradigm. After 14 days of virus and micro-LED probe implantation, we place mice
252 in a two-compartment apparatus and monitor their behaviors with a camera during
253 optogenetic modulations (Figure 3c and Figure S17). Figure 3d provides the test protocol,
254 including a baseline pretest (10 mins), red LED stimulation (pulsed wave, 30 mins), a rest
255 phase (30 mins), and blue LED stimulation (continuous wave, 30 mins). The red or blue LED
256 stimulations are only provided once the mice appear in the left chamber. Representative heat
257 maps in Figure 3e show the change of real-time behaviors during optogenetic stimulations,
258 for mice expressing different combinations of opsins. Summarized results in Figure 3f clearly
259 show that mice co-expressing ChimsonR and stGtACR2 present strong preference and
260 avoidance behaviors following red and blue stimulations, respectively. Additionally, the
261 application of both red and blue stimulations in opposite chambers further enhances the
262 preference indices of mice compared to those only experiencing single color stimulations as
263 well as the control group (co-expressing EGFP and mCherry), demonstrating the efficacy of
264 bidirectional modulation (Figure S18).

265 By contrast, the control groups without photosensitive opsins (expressing only EGFP
266 and mCherry) show little difference of behaviors under optical stimulations. More results are
267 provided in Figures S19 and S20, comparing these mice with other groups expressing only
268 ChrimsonR or stGtACR2. When introducing only ChrimsonR, mice exhibit place preference
269 under both red and blue stimulations. For the group with only stGtACR2, blue light
270 effectively evokes place aversion while red light generates little influence on mouse
271 behaviors. Figures 3g and 3h present the dynamic behavior change at different time courses.
272 These results are consistent with the spectral characteristics of the opsins as well as the *in*
273 *vitro* neural responses at the cellular level (Figure 2), elucidating the utility of bidirectional
274 modulations with wireless, dual-color micro-LED probes. In conclusion, the implantable
275 wireless dual-color LED probe combined with two spectrally distinct channelrhodopsins can
276 realize bi-directional control of the place preference or aversion in freely behaving mice.

277

278 **Bidirectional optogenetic modulation of social interactions among multiple mice, with**
279 **wireless dual-color micro-LED probes**

280 Modulating dopaminergic neurons in the VTA region also influences the social preference, in
281 particular, affective and aggressive behaviors[49, 50]. Compared with tethered stimulation
282 systems, our wirelessly operated micro-LED probes with independently addressable
283 illuminations present prominent advantages in studying social interactions among multiple
284 objects (Movie S3). Additionally, the colocalized, dual-color emission capability allows the
285 bidirectional regulation of social activities in real-time, which is difficult to access with single
286 color stimulations[49, 51]. In paired-object interactions (Figure 4a), two mice co-expressing
287 ChrimsonR and stGtACR2 in the VTA are placed in an open-field arena, and synchronized
288 red or blue stimulations are provided for 5 mins each. Mice behaviors are video recorded
289 throughout the test period, with social activities (including sniffing and attacking) labeled and

290 scored (Figure 4b). The total time spent in these activities is summarized and compared
291 among different scenarios (red light on, blue light on, and resting) in Figure 4c. In
292 comparison to the resting state, red or blue LED stimulations strongly promote or suppress
293 social interactions between two objects in the experiment group, while no significant effects
294 are observed in the control group (expressing EGFP and mCherry).

295 The wireless micro-LED probes can further be applied to interrogate more
296 complicated interaction behaviors among multiple (> 2) objects. In Figure 4d, we place three
297 mice in the same social chamber and provide these animals with alternating red or blue LED
298 stimulations. In such a testing paradigm, two mice receive red stimulations while the third
299 one receives blue stimulation, then vice versa (Figure 4e). The mice with red stimulations
300 spend more time interacting with each other compared to the individual under blue
301 illuminations, and the social preference can be reversed by alternating the stimulation
302 patterns among these three mice in real-time (Figure 4f). By contrast, summarized data
303 among control groups present no significant difference under red or blue stimulations.
304 Collectively, these social interaction explorations clearly demonstrate the unique advantage
305 of our wireless and bidirectional LED stimulators in the interrogation of complex animal
306 behaviors.

307

308 **Bidirectional optogenetic regulation of dopamine release *in vivo*, with wireless dual-**
309 **color micro-LED probes**

310 The effective bidirectional behavior manipulations demonstrated in Figures 3 and 4 can be
311 ascribed to the light-induced activation and inhibition of dopaminergic neurons in the VTA.
312 We further investigate the effect of optogenetic stimulations on dopamine release using *in*
313 *vivo* experiments described in Figure 5a. Similarly, combined opsins (ChrimsonR and

314 stGtACR2) are expressed and followed by implanting the dual-color micro-LED probe in the
315 VTA of *DAT-cre* mice. While stimulations are performed in the VTA, dopamine signals are
316 simultaneously monitored in one of its main projection areas, the nucleus accumbens
317 (NAc)[52, 53, 54]. A genetically encoded indicator $GRAB_{DA2m}$[55] is expressed in the NAc, where
318 the fluorescence signals are recorded with a fiber photometer[30, 31, 48, 49, 56, 57]. The combination
319 of micro-LED based optogenetic stimulations and fiber-based photometric recordings realizes
320 all-optical interrogation of neural circuits. During the surgery, we carefully select the
321 insertion direction of the micro-LED probe, to obtain desirable stimulation efficacy in the
322 VTA and minimize the optical crosstalk that could disturb photometric recording in the NAc
323 (Figure S21). Fluorescence images in Figure 5b show the expressions of $GRAB_{DA2m}$ in the
324 NAc as well as ChrimsonR and stGtACR2 in the VTA.

325 Figure 5c plots temporally resolved dopamine release in response to stimulations
326 caused by red and blue micro-LEDs in the same mice. Other representative curves are
327 presented in Figure S22, with results summarized in Figure 5d. Illuminating the VTA by red
328 or blue micro-LEDs (with injection currents from 0 to 10 mA) clearly induces increased or
329 decreased dopamine signals in the NAc, which correlates with neuron responses at the
330 cellular level (Figure 2). Experiments operated among mouse groups expressing different
331 opsins are also performed, with results compared in Figure 5e. In contrast to the group
332 expressing both opsins (ChrimsonR and stGtACR2), mice with only ChrimsonR show
333 increased dopamine release under both red and blue illuminations, and dopamine suppression
334 is observed under blue illumination for the mice with only stGtACR2. The control group
335 (with EGFP and mCherry) exhibits no response under optical stimulations. These results
336 evidently explain *in vivo* preference and avoidance behaviors presented in Figure 3,
337 showcasing the capability for precise control of neural activities based on bidirectional, dual-
338 color modulations.

339 We further investigate the level of the released dopamine with coincident red and blue
340 LED radiations. Figure 5f plots example traces of dopamine transients, in response to the red
341 and blue micro-LEDs under pulse and continuous operations (6-s duration) with varied
342 currents. Statistical data for accumulative dopamine concentration variations (unit: area under
343 the curve during stimulation, or AUC) are summarized in Figure 5g and Figure S23.
344 Decreasing the power of the red LED and increasing the power of the blue LED to cause the
345 decline of dopamine release. Additionally, the blue LED current required to suppress the
346 dopamine release is much lower than that of the red LED required for dopamine level rises,
347 which further conforms with the cellular activities reported in Figure 2. It should be noted
348 that the *in vivo* results in Figure 5g are not quantitatively identical to the *in vitro*
349 electrophysiological ones in Figure 2m. In fact, higher irradiances for blue LEDs are needed
350 for effective inhibition *in vivo*. This may be due to the fact that blue light has higher
351 absorption in tissue and stronger illumination is required to affect enough cells in the VTA.

352 Figure 5h (and more examples in Figure S24) presents dopamine dynamics in
353 response to alternated or combined red and blue LED stimulations, for mice expressing
354 ChrimsonR and stGtACR2. The red illumination triggers the elevated dopamine release,
355 while the use of blue light can effectively and promptly suppress the signal. Similar
356 illumination patterns are implemented on mice expressing different opsins (Figures 5i–5k)
357 and results are summarized and compared in Figures 5l–5n. Evidently, red or blue
358 illuminations bidirectionally regulate dopamine signals in the experiment group (with both
359 ChrimsonR and stGtACR2). On the other hand, mice expressing only ChrimsonR can be
360 excited by both red and blue light, and those with only stGtACR2 can only be inhibited by
361 blue light and show no reaction under red light. Finally, the control group (with EGFP and
362 mCherry) does not respond to any optical stimulation patterns. Taken together, these results
363 clearly demonstrate that wireless dual-color LED combined with optogenetics enable

364 efficient, bidirectional control of neuronal activity in the VTA and DA release of the terminal
365 in the NAc. It is also noted that fluorescence signals experience a drop when the blue LED is
366 operating during red stimulation for the mice only expressing ChrimsonR (Figure 5i). Such a
367 response is unexpected considering the fact that blue light also activates ChrimsonR. One
368 possible explanation is that when both pulsed red light and continuous blue light are imposed
369 simultaneously, their activation effects on ChrimsonR are not additive but competitive. On
370 the other hand, the application of both LEDs possibly induces additional heating effects,
371 complicating the optical and thermal responses of ChrimsonR. Nevertheless, understanding
372 spectral and temporal properties for these opsins requires further explorations in the future
373 work.

374

375 **DISCUSSION**

376 Optogenetic modulations offer a viable solution for cell-type-specific targeting, but still
377 demand biological and engineering tools for versatile functionalities. In this work, we report
378 that bidirectional optogenetic activation and inhibition in behaving mice can be achieved by
379 co-expressing spectrally distinct excitatory and inhibitory channelrhodopsins, cooperating
380 with a wireless, dual-color micro-LED probe for colocalized red and blue stimulations. With
381 collective results at the cellular, circuit, behavioral and social levels, successful proof-of-
382 concept demonstrations in the VTA-NAc circuitry in freely moving mice clearly establish the
383 utility of such a synergistic methodology.

384 The unique characteristics of thin-film, microscale optoelectronic devices, and their
385 integration strategies implicate prominent advantages over conventional waveguide-coupled
386 or single-color LED-based sources. In terms of technology developments, more directions
387 can be explored and some preliminary efforts are presented below: 1) Multiple red and blue
388 micro-LEDs can be assembled on the implantable probe via the stacking approach, realizing

389 multi-channel, bidirectional modulations imposed on multiple brain regions (Movie S4). It is
390 noted that the efficacy of preference behavior regulations demonstrated in Figure 3 would
391 also be enhanced by implementing dual-channel stimulations bilaterally in the VTA[58, 59, 60, 61].
392 2) The use of miniaturized wireless control circuits allows independently addressing multiple,
393 untethered animal objects, making the interrogations of more complex social behaviors
394 feasible[62, 63, 64, 65]. 3) Micro-LEDs with other colors can also be included and target specific
395 opsins more efficiently. For example, a tri-color probe can be achieved by similarly stacking
396 red, green, and blue micro-LEDs in a vertical structure (Movie S5). Independently controlled
397 micro-LEDs can interact with different opsins that express in the same or different
398 populations of cells. 4) Micro-LED based optogenetics can also be combined with previously
399 reported electrical, optical and chemical sensors as well as microchannel devices for drug
400 administrations[66, 67, 68, 69], achieving closed-loop neural activity stimulations and detections.
401 While arrays of blue InGaN micro-LEDs can be directly grown on silicon and integrated with
402 recording electrodes[41], the combination of simultaneous dual-color stimulations and
403 electrophysiological recordings in the deep brain region like VTA require more sophisticated
404 device design and fabrication and have not been attempted here. Considering the system
405 dimensions, wireless circuits can be further miniaturized by employing inductive coupling-
406 based power transfer strategies[24, 26]. In terms of biocompatibility, tissue lesions can be further
407 reduced by using thinner substrates with much lower stiffness[45]. Taken together, we envision
408 a multi-spectral, multi-channel, multi-objective, and multi-functional optical neural interface,
409 realizing wireless, real-time, bi-directional, close-loop, and simultaneous interrogations of
410 neural signals in living animals with desirable system stability and biocompatibility.

411 On the other hand, the efficacy of optogenetic modulations can be further optimized
412 by advanced biological engineering. Other combinations of opsins, like ChR2 and Jaws[36],
413 have also been proved to be feasible. A recent effort fuses excitatory and inhibitory

414 channelrhodopsins (ChrimsonR and GtACR2) in a single, trafficking-optimized tandem
415 protein (BiPOLES), improving the efficiency of opsin co-expression[70]. Moreover, the
416 combination of super sensitive opsins (Jaws[15], ChRmine[71], ReaChR[72], SOUL[13], etc.) could be
417 explored for bidirectional modulations via extra-cranial illumination without implants. Since
418 relatively large irradiance (> 200 mW/mm^2) is required to penetrate into the deep tissue,
419 corresponding light sources and control systems have to be miniaturized for wireless
420 operation in mice. In addition to the bidirectional modulation of the same cell population, the
421 dual-color (or even tri-color) micro-LED probe can also selectively activate genetically
422 distinct and spatially intermingled cells expressing spectrally resolved opsins (for example,
423 blue for ChR2 or GtACR2, green for C1V1 or GtACR1 and red for ChrimsonR or
424 halorhodopsin)[3, 7, 8, 21] and provide prolonged activation of neuronal activity by regulating
425 step-function opsins (for example, SSFO, SOUL)[11, 13, 73], which is also of critical importance
426 for understanding the circuit structures and functions. It should be also noted that these dual-
427 color or multi-color modulations should be carefully designed, and their efficacies are highly
428 dependent on the spectral overlap among opsins, the irradiance of different colors, levels of
429 viral expressions, etc. Possible applications would include bidirectional modulations of neural
430 activities by leveraging electrophysiological or neurotransmitter signals for medications of
431 seizures or Parkinson's disease[29, 74]. Besides the brain system, the spinal cord and peripheral
432 neural circuits can also be targeted for medical treatments[75, 76, 77]. In summary, the results
433 presented here provide a viable means for fundamental neuroscience studies and advanced
434 neuroengineering applications.

Methods

Device Fabrication

Fabrication of red and blue micro-LEDs

Details about the thin-film micro-LED structures and fabrication processes can be found in our previous work[37, 39]. Via metal-organic chemical vapor deposition (MOCVD), red and blue LEDs are originally grown on gallium arsenide (GaAs) and sapphire substrates, respectively. The red LED active device contains an indium gallium phosphide (InGaP) based multiple quantum well structure (thickness ~5.6 μm) grown on GaAs with an $Al_{0.95}Ga_{0.05}As$ sacrificial interlayer. The blue LED active device contains an indium gallium nitride (InGaN) based multiple quantum well structure (thickness ~7 μm) grown on sapphire. Photolithographic process, wet/dry etching and metallic electrode deposition define the LED geometry (size ~180 μm × 125 μm). Freestanding, thin-film red LEDs are formed by selectively removing the $Al_{0.95}Ga_{0.05}As$ sacrificial layer in a hydrofluoric acid (HF) based solution. Freestanding, thin-film blue LEDs are formed by a laser lift-off (with a KrF excimer laser at 248 nm). Poly(dimethylsiloxane) (PDMS) based stamps are employed to pick up released thin-film micro-LEDs and transfer them onto other foreign substrates.

Fabrication of thin-film filters

Details about the thin-film filter fabrication can be found in our previous work[40]. The wavelength selective thin-film filters is based on a multilayered titanium dioxide (TiO_2) and silicon dioxide (SiO_2) structure (thickness ~ 6.6 μm) comprising (from top to bottom): 19 nm TiO_2 / 15 periods (89 nm SiO_2 + 52 nm TiO_2) / 63 nm SiO_2 / 66 nm TiO_2 / 22 periods of (73 nm SiO_2 + 42.5 nm TiO_2) / 154 nm SiO_2. The structure is deposited on GaAs by ion beam-assisted sputter deposition. The filter shape (size ~ 180 μm × 125 μm) is defined by laser milling (Nd: YVO_4 laser, 1064 nm). After removing the GaAs substrate in solutions (NH_4OH:

459 H_2O_2: H_2O = 1:1:2), freestanding thin-film filters can be picked up and transferred printed
460 onto other foreign substrates by PDMS stamps.

461 *Fabrication of dual-color micro-LED probes*

462 The process flow to fabricate the dual-color micro-LED probe is described in Figure S1. The
463 micro-LED probe is based on a flexible substrate made of composite polyimide (PI) and
464 copper (Cu) films (from top to bottom: Cu/PI/Cu = 18/25/18 μm, from DuPont). From bottom
465 to top, a red LED, an optical filter and a blue LED are sequentially transferred printed on the
466 film by PDMS in a vertical stack, via a customized alignment setup (with a lateral alignment
467 accuracy of ~2 μm). Between each device layer, spin-coated SU-8 based epoxy (thickness ~
468 2–5 μm) serves an optically transparent and electrically insulating bonding layer. Each
469 individual LED is metalized with sputtered metal layers (Cr/Au/Cu/Au = 10/100/500/100
470 nm). Laser milling (ultraviolet laser 365 nm) defines the needle shape (width ~320 μm,
471 length ~5 mm). A bilayer of PDMS (~20 μm, by dip-coating) and parylene (~15 μm, by
472 CVD) is used for waterproof encapsulation. For comparison in Figure 1g, laterally arranged
473 red-blue micro-LED probes are also fabricated with similar procedures.

474 **Device Characterization and Modeling**

475 *Structural and optoelectronic characterizations*

476 Scanning electron microscopic (SEM) images are taken with a ZEISS Auriga SEM / FIB
477 Crossbeam System. Optical images are captured by a microscope MC-D800U(C). The LED
478 emission spectra are measured with a spectrometer (HR2000+, Ocean Optics). Current-
479 voltage characteristics are recorded by a Keithley 2400 source meter. LED irradiances and
480 external quantum efficiencies are measured using a spectroradiometer with an integrating
481 sphere (LabSphere Inc.). The angular-dependent emission profiles are measured by a
482 standard Si photodetector (DET36A, Thorlabs) with the device mounted on a goniometer.

483 The probe's mechanical properties are measured with dynamic mechanical analysis (DMA
484 Q800, TA Instruments). For *in vitro* tests, micro-LED probes are implanted into the brain
485 phantom. The brain phantom is made of agarose (0.5% w/v), hemoglobin (0.2% w/v), and
486 intralipid (1% w/v) mixed in phosphate buffer solutions (98.3% w/v). After stirring, the
487 mixed liquid is heated to boiling and then naturally cooled to room temperature, forming the
488 gels.

489 *Optical modeling*

490 A ray-tracing method based on Monte Carlo simulations (TracePro free trial version) is used
491 to simulate the light propagation in the brain tissue. In the model, the tissue (size 5 × 5 × 5
492 mm^3) has absorption coefficients of 0.2 /mm and 0.08 /mm, and scattering coefficients of 47
493 /mm and 35 /mm, for blue (475 nm) and red (630 nm) wavelengths, respectively. The tissue
494 has an anisotropy factor of 0.85 and a refractive index of 1.36[78]. Planar sources similar to the
495 surface of micro-LEDs (size 125 × 180 μm^2) emit 10^6 rays for each monochromic wavelength
496 (475 nm and 630 nm), assuming a Lambertian distribution. For the stacked micro-LEDs, the
497 blue and red sources are overlaid. For the lateral case, the two sources are adjacent to each
498 other.

499 *Thermal characterizations*

500 For *in vitro* experiments, the micro-LED probes are implanted into the brain phantom (~0.5
501 mm underneath the surface, at a depth of ~5 mm), and various currents are injected into the
502 LEDs. The temperature distributions on the phantom surface are mapped with an infrared
503 camera (FOTRIC 228). For comparison, the temperature inside the phantom is also measured
504 by inserting an ultra-fine flexible micro thermocouple (Physitemp, IT-24P) (~0.3 mm above
505 the LED probe tip). For *in vivo* experiments, the micro-LED probe is bonded with the same

506 thermocouple and inserted into the anesthetized mouse brain. Steady-state temperature rises
507 are recorded from the thermocouple with a thermometer (Physitemp, BAT-12).

508 *Thermal modeling*

509 3D steady-state heat transfer models are established by finite element analysis (Comsol
510 Multiphysics). Materials and corresponding parameters (density, thermal conductivity and
511 heat capacity) used in the model include: brain tissue (1.1 g/cm^3, 0.5 W/m/K, 3.7 J/g/K),
512 parylene (1.2 g/cm^3, 0.082 W/m/K, 0.71 J/g/K), PDMS (0.98 g/cm^3, 0.16 W/m/K, 1.5 J/g/K),
513 polyimide (1.4 g/cm^3, 0.15 W/m/K, 1.1 J/g/K), GaN (6.1 g/cm^3, 130 W/m/K, 0.49 J/g/K), Cu
514 (9.0 g/cm^3, 400 W/m/K, 0.39 J/g/K), SU-8 (1.2 g/cm^3, 0.2 W/m/K, 1.2 J/g/K), GaP (4.4
515 g/cm^3, 110 W/m/K, 0.43 J/g/K). The boundary condition is natural heat convection to air at
516 20 °C. The micro-LED probe serves as the heat source, with the input thermal power
517 estimated by $P = V \times I \times (1 - \mathrm{EQE})$, where V, I, and EQE are the measured voltage, current,
518 and corresponding external quantum efficiencies for LEDs. The thermocouple is also
519 included in the model for comparison, which is 0.3 mm above the LED probe tip. It consists
520 of two metal wires: copper (diameter 31 μm) and constantan (45Ni-55Cu alloy, thermal
521 conductivity 21 W/m/K, diameter 31 μm), which are encapsulated by polyester to form a wire
522 with an outer diameter of 127 μm.

523

524 **Wireless Circuit Design**

525 A customized circuit module is designed to wirelessly operate the implantable micro-LED
526 probe by independently controlling the red and the blue micro-LEDs for bi-directional
527 modulation. The schematic diagram is depicted in Figure S5, with a detailed circuit diagram,
528 layouts, and components presented in Figures S6–S9. The core components include: a micro-
529 controller (nRF24LE1, Nordic Semiconductor) operated at 2.4 GHz for data communication,

530 and two LED drivers (ZLED7012, Renesas Electronics Corp.) with programmable current
531 levels, frequencies, pulse widths for providing a constant current to micro-LEDs[38]. The driver
532 provides programmable constant current levels ranging from 1.8 mA to 20 mA and also
533 supports arbitrary waveforms. Two red LEDs are used on the circuit board outside the brain
534 for signal indication, without affecting the mouse behaviors[79]. Control signals are wirelessly
535 transmitted from the transmitting module connected to a laptop computer via an antenna
536 operating at a radio frequency of 2.4 GHz, with a communication distance up to 50 m.
537 Different from our previous design[80], here a polyimide-based flexible circuit board is
538 implemented for reduced weight. The wireless circuit has a footprint of ~2.2 cm × 1.3 cm and
539 a weight of 1.9 g (including a 0.9-g rechargeable lithium-ion battery with a capacity of 35
540 mAh). Used in the experimental conditions in this paper, the battery life can reach up to 2
541 hours. The circuit can be connected with the implanted micro-LED probes via a flexible
542 printed circuit (FPC) connector before the animal experiment (Figure S8).

543

544 **Biological Studies**

545 *Animals*

546 Animal care is in accordance with the institutional guidelines of National Institute of
547 Biological Sciences in Beijing (NIBS), with protocols proved by Institutional Animal Care
548 and Use Committee (IACUC). All mice are socially housed in a 12 h/12 h (lights on at 8 am)
549 light/dark cycle, with food and water *ad alibitum*. Wildtype, male C57BL6/N mice are
550 purchased from VitalRiver (Beijing, China). *DAT-Cre* (B6.SJLSlc6a3tm1.1(cre) Bkmn; JAX
551 Strain 006660) and *CamkIIa-Cre* (B6.Cg-Tg(Camk2a-cre)T29-1Stl/J; JAX Strain 005359)
552 mice are at least six weeks old at the time of surgery.

553 *Virus production*

554 The AAV2/9-CAG-DIO-ChrimsonR-tdTomato (Plasmid #130909) vector[7] is from Addgene.
555 The AAV2/9-EF1a-DIO-stGtACR2-EGFP-Kv2.1 plasmid is synthesized and constructed
556 according to the original reports[8, 9]. The AAV-hSyn-$GRAB_{DA2m}$ plasmid is provided by Prof.
557 Yulong Li at Peking University[55]. AAV vectors are packaged into serotype2/9 vectors, which
558 consist of AAV2 ITR genomes pseudotyped with AAV9 serotype capsid proteins. AAV
559 vectors are replicated in HEK293 cells with the triple plasmid transfection system and
560 purified by chloroform[81], resulting in AAV vector titers of about 5×10^{12} particles/mL. Virus
561 suspension is aliquoted and stored at −80 °C. AAV titers are measured using real-time qPCR.
562 Adeno-associated viral particles are produced at the Vector Core Facility at Chinese Institute
563 for Brain Research, Beijing (CIBR).

564 *Stereotaxic Surgery*

565 Adult *DAT-Cre* mice are anesthetized with an intraperitoneal injection of Avertin (250 mg/kg)
566 before surgery and then placed in a standard stereotaxic instrument for surgical implantation
567 (Figure S12). After disinfection with 0.3% hydrogen peroxide, a small incision of the scalp is
568 created to expose the skull. Then, 0.3% hydrogen peroxide is applied to clean the skull. A
569 small craniotomy is made, followed by carefully removing the dura with a thin needle. A
570 calibrated pulled-glass pipette (Sutter Instrument) is lowered to the VTA (coordinates 3.64
571 mm posterior to the bregma, 0.5 mm lateral to the midline, and 4.6 mm ventral to the skull
572 surface). The virus is delivered through a small durotomy by a glass micropipette using a
573 microsyringe pump (Nanoliter 2000 injector with the Micro4 controller, WPI).

574 Four different combinations of virus are used for *in vivo* experiments:

575 1) ChrimsonR + stGtACR2 (AAV2/9-CAG-DIO-ChrimsonR-tdTomato and AAV2/9-EF1a-
576 DIO-stGtACR2-EGFP-Kv2.1, 1:1);

577 2) mCherry + EGFP (AAV2/9-EF1a-DIO-mCherry and AAV2/9-EF1a-DIO-EGFP, 1:1);

578 3) ChrimsonR + EGFP (AAV2/9-CAG-DIO-ChrimsonR-tdTomato and AAV2/9-EF1a-DIO-
579 EGFP, 1:1)

580 4) stGtACR2 + mCherry (AAV2/9-EF1a-DIO-stGtACR2-EGFP-Kv2.1 and AAV2/9-EF1a-
581 DIO-mCherry, 1:1)

582

583 A bolus of 0.4 μL of mixed virus is injected into the VTA at 46 nL/min. The pipette is held in
584 place for 10 min after the injection and then slowly withdrawn. For the real-time place
585 preference (RTPP) behavioral test, the dual-color LED probe implantation is carried out after
586 virus injection and diffusion. The probe was slowly implanted at the side of the target brain
587 areas with an angle of 45° to midline (coordinates 3.64 mm posterior to the bregma, 0.8 mm
588 lateral to the midline, and 4.85 mm ventral to the skull surface). The probe is fixed to the
589 skull with dental cement. For dopamine detection with fiber photometric recording, the AAV-
590 hSyn-GRAB$_{DA2m}$ (0.2 μL) is injected into the NAc (coordinates: 1.18 mm front to the
591 bregma, 0.75 mm lateral to the midline, and 3.75 mm ventral to the skull surface). Optical
592 fiber implantation is carried out after virus injection and diffusion. A piece of optical fiber
593 (FT200UMT, 200 μm O.D., 0.39 NA, Thorlabs) is fit into an LC-sized ceramic fiber ferrule
594 (Shanghai Fiblaser, China) and implanted over the target brain areas with the tip 0.1 mm
595 above the virus injection sites in the NAc. The ceramic ferrule is fixed to the skull with
596 Cyanoacrylate adhesive (TONSAN 1454) and dental cement. After the virus injection and
597 device implantation, mice are housed individually to prevent potential damage to the probe.
598 All subsequent experiments are performed at least 2 weeks after injection to allow sufficient
599 time for transgene expression and animal recovery.

600 *Immunohistochemistry*

601 The micro-LED probes are implanted into the VTA region and fixed to the skull with
602 Cyanoacrylate adhesive (TONSAN 1454) and dental cement. After 1 day or 3 weeks
603 following the surgery, mice are sacrificed with an overdose of pentobarbital and
604 transcardially perfused with 0.1M phosphate buffer saline and 4% paraformaldehyde. After
605 pcryoprotection in 30% sucrose, brains are post fixed in 4% PFA for 4 hours and 30%
606 sucrose for 24 hours, 40-μm-thick coronal sections are prepared by a cryostat (Leica
607 CM1950). After 5-min PBS rinses for 3 times, the sections are blocked in PBST (PBS + 0.3%
608 Triton X-100) with 3% bovine serum albumin for 1 hour, and incubated in rabbit anti-Iba1
609 (1:1000, Wako, Cat.#019-19741) and chicken anti-GFAP antibody (1:2000, Sigma,
610 Cat#AB5541) dissolved in PBST at 4 °C for 24 hours. After 5-min washes in PBS for 5 times,
611 the sections are incubated with Alexa Cy3-conjugated goat anti-rabbit antibody (1:500,
612 Jackson ImmunoResearch) and Alexa 488 goat anti-chicken antibody (1:500, Thermo Fisher
613 Scientific) dissolved in PBST for 2 hours at room temperature followed by 5-min washes in
614 PBS for 3 times. Finally, the samples are cover slipped in 50% glyceroland slides and
615 photographed with an automated slide scanner (VS120 Virtual Slide, Olympus) or a confocal
616 scanning microscope (DigitalEclipse A1, Nikon). The numbers of DAPI, stGtACR2 and
617 ChrimsonR stained cells or the numbers of Iba1+ microglia and GFAP+ astrocytes are
618 analyzed with Fiji software (https://fiji.sc/) and their percentages in cell population indicated
619 by DAPI are calculated.

620 *In vitro optogenetics evaluation*

621 Electrophysiological properties of the neurons in brain slices are measured with whole-cell
622 patch-clamp recording technique following a previously described procedure[31]. After two
623 weeks of virus expression (ChrimsonR + stGtACR2), mice are deeply anesthetized with
624 pentobarbital (100 mg/kg i.p.) and intracardially perfused with 5 mL ice-cold oxygenated
625 modified artificial cerebrospinal fluid (ACSF) at a rate of 2 mL/min. After perfusion with

626 modified ACSF containing (in mM): 225 sucrose, 119 NaCl, 2.5 KCl, 0.1 $CaCl_2$, 4.9 $MgCl_2$,
627 1.0 NaH_2PO_4, 26.2 $NaHCO_3$, 1.25 glucose, 3 kynurenic acid, and 1 Na L-ascorbate (Sigma-
628 Aldrich), brains are quickly removed and placed in ice-cold oxygenated ACSF containing (in
629 mM): 110 choline chloride, 2.5 KCl, 0.5 $CaCl_2$, 7 $MgCl_2$, 1.3 NaH_2PO_4, 25 $NaHCO_3$, 20
630 glucose, 1.3 Na ascorbate, and 0.6 Na pyruvate. Sagittal sections (200 μm thick) are prepared
631 using a Leica VT1200S vibratome. Brain slices are incubated for 1 hour at 34 °C with ACSF
632 saturated with 95% O_2/5% CO_2 and containing (in mM) 125 NaCl, 2.5 KCl, 2 $CaCl_2$, 1.3
633 $MgCl_2$, 1.3 NaH_2PO_4, 25 $NaHCO_3$, 10 glucose, 1.3 Na ascorbate, and 0.6 Na pyruvate. The
634 internal solution within whole-cell recording pipettes (3–6 MΩ) contains (in mM): 130 K-
635 gluconate, 10 HEPES, 0.6 EGTA, 5 KCl, 3 Na_2ATP, 0.3 Na_3GTP, 4 $MgCl_2$, and 10 Na_2-
636 phosphocreatine (pH 7.2–7.4). Voltage-clamp recordings are performed using a MultiClamp
637 700B amplifier (Molecular Devices). Traces are low-pass filtered at 2.6 kHz and digitized at
638 10 kHz (DigiData 1440, Molecular Devices). The data are acquired and analyzed using
639 Clampfit 10.0 software (Molecular Devices). Red and blue illuminations are provided by a
640 fiber-coupled to two laser sources (633 nm and 473 nm).

641 *In vivo extracellular electrophysiology recordings*

642 We perform the extracellular single-unit recording as our previously described procedure[82].
643 Adult CamkIIa-Cre mice are anesthetized with an intraperitoneal injection of Avertin (250
644 mg/Kg). A bolus of 1 μL of virus (AAV2/9-CAG-DIO-ChrimsonR-tdTomato and AAV2/9-
645 EF1a-DIO-stGtACR2-EGFP-Kv2.1, 1:1) is injected into neocortex and hippocampus at
646 different depths (AP −1.6 mm, ML 1.1 mm, DV 0.4 to 2.0 mm increments; 200 nL/site). A
647 silver wire (127 μm diameter, A-M system) is attached to a skull-penetrating M1 screw above
648 the olfactory bulb to serve as the ground reference. For head-fixed preparations, a custom-
649 made titanium head-plate is secured to the skull with dental acrylic. Recordings are
650 performed 2 weeks after viral injection. Mice are held in place with a header bar cemented to

651 the skull. The dual-color micro-LED probe is lowered into the neocortex with a 15° angle
652 from medial to lateral and another 10° angle from anterior to posterior. 8 stereotrodes with Pt-
653 Ir wires (diameter 17.5 μm, platinum 10% iridium, California Fine Wire, USA) are used for
654 extracellular electrophysiology recordings. The distance between the stereotrodes and the
655 micro-LEDs is ~500 μm. To reduce the noise induced by the stray capacitance coupling from
656 LEDs to electrodes, we use a tinfoil shield to encompass the electric circuit of the LED.
657 Voltage signals are digitized and recorded by an Open-Ephys board (http://www.open-
658 ephys.org/). Signals from each recording electrode are band-pass-filtered between 300 and
659 6000 Hz and sampled at 25 kHz. Single units are discriminated with principal component
660 analysis (Offline sorter, spike2, CED, UK). Recorded units smaller than 2.5 times the noise
661 band or in which interspike intervals are shorter than 2 ms are excluded from further analysis.
662 Red light (pulse width 0.2 s, interval 3 s, 50–100 pulses, LED current 10 mA) and blue light
663 (pulse width 1 s, interval 3 s, 50–100 pulses, LED current 1 mA) are used to activate or
664 inhibit neurons. Data are analyzed and plotted with a custom-developed MATLAB program.

665 *Calcium imaging in acute brain slice*

666 Mice are injected with 0.4 μL of Raav2/9-hsyn-GCaMP6m into the S1. After 2 weeks of
667 recovery, acute brain slices are prepared. Ca^{2+} fluorescent signals in GCaMP6m expressing
668 cells are captured with a 20× water immersion objective on a confocal microscope (FV1000,
669 Olympus). For cell activation, 1 μM α-amino-3-hydroxy-5-methyl-4-isoxazolepropionic acid
670 (AMPA, No.A6816, Sigma-Aldrich) is added in ACSF to enhance the Ca^{2+} signals. Control
671 experiments are performed by applying pure ACSF. Fluorescence images are analyzed via
672 ImageJ. Normalized fluorescence changes are calculated as $dF/F = (F - F_0) / F_0$, where F_0 is
673 the baseline intensity (before 10 s).

674 *Real-time place preference test*

675 After 2 weeks of recovery and AAV expression in *DAT-cre* mice, real-time place
676 preference/avoidance (RTPP) tests are performed in a custom-made two-compartment
677 apparatus. The RTPP apparatus comprises two white plastic chambers (size: 25 × 25 × 30, L
678 × W × H in cm), separated by half-open opaque plastic walls in the middle (8 × 30, L × H
679 cm). An RTPP test consists of 3 phases: 10-min baseline (pretest), 30-min red LED
680 stimulation, 30-min rest (no stimulation), and 30-min blue LED simulation. During the
681 pretest phase, individual mice are allowed to freely explore the entire apparatus for 10 min.
682 Mice that exhibit a strong initial preference or avoidance for one of the side chambers
683 (preference index > 60% or < 40%) are excluded from further experiments. During the red
684 LED stimulation phase, mice that entered the left chamber received red light pulses (20 Hz,
685 20-ms pulse, 7 mA). During the blue light stimulation phase, mice that entered the left
686 chamber receive constant blue light (continuous, 5 mA). The locomotion of mice is assessed
687 from the video recording data using a custom-developed MATLAB program.

688 *Social interaction test*

689 After 2 weeks of recovery and AAV expression, social interaction tests are performed with
690 *DAT-cre* mice. Two or three mice are placed in an open-field arena (30 × 30 cm^2), wireless
691 dual-color micro-LED probes provide red (20 Hz, 20-ms pulse, 7 mA) and blue (continuous,
692 5 mA) stimulations, and their behaviors are recorded by a camera. In paired-mice
693 experiments, the two mice receive the same 3-phase stimulations: 1) 5-min baseline (pretest,
694 no stimulation), 5-min red LED stimulation, 5-min free interaction (no stimulation), and 5-
695 min red LED simulation; 2) 2-hour rest in individual housing; 3) 5-min baseline (pretest, no
696 stimulation), 5-min blue LED stimulation, 5-min free interaction (no stimulation), and 5-min
697 blue LED simulation. For triple-mice interactions, the three mice receive the following
698 stimulations: 5-min baseline (pretest, no stimulation), 5-min LED stimulation (red, red, blue),
699 5-min free interaction (no stimulation), and 5-min LED simulation (blue, blue, red). The tests

700 are repeated three times, by alternating the order. Experiment groups express stGtACR2 +
701 ChrimsonR, and control groups express EGFP + mCherry. The videos are analyzed by Etho
702 Vision XT 15 and social behaviors including sniff and attack are manually labeled and
703 scored.

704 *Fiber photometry for dopamine (DA) detection*

705 Details for the fiber photometric system are described previously[82]. The excitation source is a
706 488 nm semiconductor laser (Coherent, Inc. OBIS 488 LS, tunable power up to 60 mW). A
707 dichroic mirror with a 452–490 nm reflection band and a 505–800 nm transmission band
708 (Thorlabs, Inc. MD498) is employed for wavelength selection. A multimode fiber (Thorlabs,
709 Inc., 200 μm in diameter and 0.39 in numerical aperture) coupled to an objective lens
710 (Olympus, 10×, NA 0.3) is used for optical transmission. The fluorescence signals are
711 collected with a photomultiplier tube (PMT) (Hamamatsu, Inc. R3896) after filtering by a
712 GFP bandpass filter (Thorlabs, MF525-39). An amplifier (C7319, Hamamatsu) is used to
713 convert the current output from the PMT to voltage signals, which are further filtered through
714 a lowpass filter (40 Hz cut-off; Brownlee 440, USA). The fluorescence signals are digitalized
715 at 100 Hz and recorded by a Power 1401 digitizer and Spike2 software (CED, UK).
716 Photometric data are exported and analyzed with MATLAB. The fluorescence signals ($\Delta F/F_0$)
717 are processed by averaging the baseline signal F_0 over a 4.5-s long control time window and
718 presented as heatmaps or per-event plots. AUC (area under the curve) of the DA signal is
719 used for statistical analysis. AUC is the integral of a curve that describes the variation of DA
720 signals during light stimulation.

721 **REFERENCES**

722 1. Won SM, Song E, Reeder JT, Rogers JA. Emerging modalities and implantable
723 technologies for neuromodulation. *Cell* 2020, **181**(1)**:** 115-135.

724 2. Vázquez-Guardado A, Yang Y, Bandodkar AJ, Rogers JA. Recent advances in
725 neurotechnologies with broad potential for neuroscience research. *Nat. Neurosci.*
726 2020, **23**(12)**:** 1522-1536.

727 3. Boyden ES, Zhang F, Bamberg E, Nagel G, Deisseroth K. Millisecond-timescale,
728 genetically targeted optical control of neural activity. *Nat. Neurosci.* 2005, **8**(9)**:**
729 1263-1268.

730 4. Zhang F, Wang L-P, Brauner M, Liewald JF, Kay K, Watzke N*, et al.* Multimodal
731 fast optical interrogation of neural circuitry. *Nature* 2007, **446**(7136)**:** 633-639.

732 5. Yizhar O, Fenno LE, Davidson TJ, Mogri M, Deisseroth K. Optogenetics in neural
733 systems. *Neuron* 2011, **71**(1)**:** 9-34.

734 6. Chow BY, Han X, Dobry AS, Qian X, Chuong AS, Li M*, et al.* High-performance
735 genetically targetable optical neural silencing by light-driven proton pumps. *Nature*
736 2010, **463**(7277)**:** 98-102.

737 7. Klapoetke NC, Murata Y, Kim SS, Pulver SR, Birdsey-Benson A, Cho YK*, et al.*
738 Independent optical excitation of distinct neural populations. *Nat. Methods* 2014,
739 **11**(3)**:** 338-346.

740 8. Govorunova EG, Sineshchekov OA, Janz R, Liu X, Spudich JL. Natural light-gated
741 anion channels: A family of microbial rhodopsins for advanced optogenetics. *Science*
742 2015, **349**(6248)**:** 647.

743 9. Mahn M, Gibor L, Patil P, Cohen-Kashi Malina K, Oring S, Printz Y*, et al.* High-
744 efficiency optogenetic silencing with soma-targeted anion-conducting
745 channelrhodopsins. *Nat. Commun.* 2018, **9**(1)**:** 4125.

746 10. Zhang F, Prigge M, Beyriere F, Tsunoda SP, Mattis J, Yizhar O*, et al.* Red-shifted
747 optogenetic excitation: a tool for fast neural control derived from Volvox carteri. *Nat.*
748 *Neurosci.* 2008, **11**(6)**:** 631-633.
749 11. Berndt A, Yizhar O, Gunaydin LA, Hegemann P, Deisseroth K. Bi-stable neural state
750 switches. *Nat. Neurosci.* 2009, **12**(2)**:** 229-234.
751 12. Hochbaum DR, Zhao Y, Farhi SL, Klapoetke N, Werley CA, Kapoor V*, et al.* All-
752 optical electrophysiology in mammalian neurons using engineered microbial
753 rhodopsins. *Nat. Methods* 2014, **11**(8)**:** 825-833.
754 13. Gong X, Mendoza-Halliday D, Ting JT, Kaiser T, Sun X, Bastos AM*, et al.* An ultra-
755 sensitive step-function opsin for minimally invasive optogenetic stimulation in mice
756 and macaques. *Neuron* 2020, **107**(1)**:** 38-51.
757 14. Brown J, Behnam R, Coddington L, Tervo DGR, Martin K, Proskurin M*, et al.*
758 Expanding the optogenetics toolkit by topological inversion of rhodopsins. *Cell* 2018,
759 **175**(4)**:** 1131-1140.
760 15. Chuong AS, Miri ML, Busskamp V, Matthews GAC, Acker LC, Sørensen AT*, et al.*
761 Noninvasive optical inhibition with a red-shifted microbial rhodopsin. *Nat. Neurosci.*
762 2014, **17**(8)**:** 1123-1129.
763 16. Schild LC, Glauser DA. Dual Color Neural Activation and Behavior Control with
764 Chrimson and CoChR in Caenorhabditis elegans. *Genet.* 2015, **200**(4)**:** 1029-1034.
765 17. Maimon BE, Sparks K, Srinivasan S, Zorzos AN, Herr HM. Spectrally distinct
766 channelrhodopsins for two-colour optogenetic peripheral nerve stimulation. *Nat.*
767 *Biomed. Eng.* 2018, **2**(7)**:** 485-496.
768 18. Lu Y, Truccolo W, Wagner FB, Vargas-Irwin CE, Ozden I, Zimmermann JB*, et al.*
769 Optogenetically induced spatiotemporal gamma oscillations and neuronal spiking
770 activity in primate motor cortex. *J. Neurosci.* 2015, **113**(10)**:** 3574-3587.

771 19. Galvan A, Caiola MJ, Albaugh DL. Advances in optogenetic and chemogenetic
772 methods to study brain circuits in non-human primates. *J. Neural. Transm.* 2018,
773 **125**(3)**:** 547-563.
774 20. Park S, Loke G, Fink Y, Anikeeva P. Flexible fiber-based optoelectronics for neural
775 interfaces. *Chem. Rev.* 2019, **48**(6)**:** 1826-1852.
776 21. Yizhar O, Fenno LE, Prigge M, Schneider F, Davidson TJ, O'Shea DJ*, et al.*
777 Neocortical excitation/inhibition balance in information processing and social
778 dysfunction. *Nature* 2011, **477**(7363)**:** 171-178.
779 22. Kampasi K, English DF, Seymour J, Stark E, McKenzie S, Voroslakos M*, et al.* Dual
780 color optogenetic control of neural populations using low-noise, multishank
781 optoelectrodes. *Microsyst. Nanoeng.* 2018, **4:** 1-16.
782 23. Kim T-i, McCall JG, Jung YH, Huang X, Siuda ER, Li Y*, et al.* Injectable, Cellular-
783 Scale Optoelectronics with Applications for Wireless Optogenetics. *Science* 2013,
784 **340**(6129)**:** 211.
785 24. Montgomery KL, Yeh AJ, Ho JS, Tsao V, Mohan Iyer S, Grosenick L*, et al.*
786 Wirelessly powered, fully internal optogenetics for brain, spinal and peripheral
787 circuits in mice. *Nat. Methods.* 2015, **12**(10)**:** 969-974.
788 25. Wentz CT, Bernstein JG, Monahan P, Guerra A, Rodriguez A, Boyden ES. A
789 wirelessly powered and controlled device for optical neural control of freely-behaving
790 animals. *J. Neural. Eng.* 2011, **8**(4)**:** 046021.
791 26. Shin G, Gomez AM, Al-Hasani R, Jeong YR, Kim J, Xie Z*, et al.* Flexible Near-Field
792 Wireless Optoelectronics as Subdermal Implants for Broad Applications in
793 Optogenetics. *Neuron* 2017, **93**(3)**:** 509-521.

794 27. Kim CY, Ku MJ, Qazi R, Nam HJ, Park JW, Nam KS*, et al.* Soft subdermal implant
795 capable of wireless battery charging and programmable controls for applications in
796 optogenetics. *Nat. Commun.* 2021, **12**(1)**:** 535.
797 28. Hashimoto M, Hata A, Miyata T, Hirase H. Programmable wireless light-emitting
798 diode stimulator for chronic stimulation of optogenetic molecules in freely moving
799 mice. *Neurophotonics* 2014, 1**:** 011002.
800 29. Wykes RC, Kullmann DM, Pavlov I, Magloire V. Optogenetic approaches to treat
801 epilepsy. *J. Neurosci. Methods.* 2016, **260:** 215-220.
802 30. Li Y, Zeng J, Zhang J, Yue C, Zhong W, Liu Z*, et al.* Hypothalamic circuits for
803 predation and evasion. *Neuron* 2018, **97**(4)**:** 911-924.
804 31. Lu L, Ren Y, Yu T, Liu Z, Wang S, Tan L*, et al.* Control of locomotor speed, arousal,
805 and hippocampal theta rhythms by the nucleus incertus. *Nat. commun.* 2020, **11**(1)**:** 1-
806 16.
807 32. Roseberry TK, Lee AM, Lalive AL, Wilbrecht L, Bonci A, Kreitzer AC. Cell-Type-
808 Specific Control of Brainstem Locomotor Circuits by Basal Ganglia. *Cell* 2016,
809 **164**(3)**:** 526-537.
810 33. Gradinaru V, Zhang F, Ramakrishnan C, Mattis J, Prakash R, Diester I*, et al.*
811 Molecular and cellular approaches for diversifying and extending optogenetics. *Cell*
812 2010, **141**(1)**:** 154-165.
813 34. Stuber GD, Sparta DR, Stamatakis AM, van Leeuwen WA, Hardjoprajitno JE, Cho S*,*
814 *et al.* Excitatory transmission from the amygdala to nucleus accumbens facilitates
815 reward seeking. *Nature* 2011, **475**(7356)**:** 377-380.
816 35. Kampasi K, Stark E, Seymour J, Na K, Winful HG, Buzsáki G*, et al.* Fiberless
817 multicolor neural optoelectrode for in vivo circuit analysis. *Sci. Rep.* 2016, **6**(1)**:** 1-13.

818 36. Noked O, Levi A, Someck S, Amber-Vitos O, Stark E. Bidirectional Optogenetic
819 Control of Inhibitory Neurons in Freely-Moving Mice. *IEEE. Trans. Biomed. Eng.*
820 2021, **68**(2)**:** 416-427.
821 37. Li L, Liu C, Su Y, Bai J, Wu J, Han Y*, et al.* Heterogeneous Integration of Microscale
822 GaN Light-Emitting Diodes and Their Electrical, Optical, and Thermal
823 Characteristics on Flexible Substrates. *Adv. Mater. Technol.* 2018, **3**(1)**:** 1700239.
824 38. Zhao Y, Liu C, Liu Z, Luo W, Li L, Cai X*, et al.* Wirelessly Operated, Implantable
825 Optoelectronic Probes for Optogenetics in Freely Moving Animals. *IEEE. Trans.*
826 *Electron. Devices.* 2019, **66**(1)**:** 785-792.
827 39. Ding H, Lu L, Shi Z, Wang D, Li L, Li X*, et al.* Microscale optoelectronic infrared-
828 to-visible upconversion devices and their use as injectable light sources. *Proc. Natl.*
829 *Acad. Sci. U.S.A.* 2018, **115**(26)**:** 6632-6637.
830 40. Liu C, Zhang Q, Wang D, Zhao G, Cai X, Li L*, et al.* High Performance,
831 Biocompatible Dielectric Thin-Film Optical Filters Integrated with Flexible
832 Substrates and Microscale Optoelectronic Devices. *Adv. Opt. Mater.* 2018, **6**(15)**:**
833 1800146.
834 41. Wu F, Stark E, Ku P-C, Wise Kensall D, Buzsáki G, Yoon E. Monolithically
835 Integrated μLEDs on Silicon Neural Probes for High-Resolution Optogenetic Studies
836 in Behaving Animals. *Neuron* 2015, **88**(6)**:** 1136-1148.
837 42. Scharf R, Tsunematsu T, McAlinden N, Dawson MD, Sakata S, Mathieson K. Depth-
838 specific optogenetic control in vivo with a scalable, high-density μLED neural probe.
839 *Sci. Rep.* 2016, **6**(1)**:** 28381.
840 43. Olivier F, Tirano S, Dupré L, Aventurier B, Largeron C, Templier F. Influence of
841 size-reduction on the performances of GaN-based micro-LEDs for display
842 application. *J. Lumin.* 2017, **191:** 112-116.

843 44. Oh JT, Lee SY, Moon YT, Moon JH, Park S, Hong KY*, et al.* Light output
844 performance of red AlGaInP-based light emitting diodes with different chip
845 geometries and structures. *Opt. Express* 2018, **26**(9)**:** 11194-11200.
846 45. He F, Lycke R, Ganji M, Xie C, Luan L. Ultraflexible Neural Electrodes for Long-
847 Lasting Intracortical Recording. *iScience* 2020, **23**(8): 101387.
848 46. Lammel S, Lim BK, Malenka RC. Reward and aversion in a heterogeneous midbrain
849 dopamine system. *Neuropharmacology* 2014, **76:** 351-359.
850 47. Morales M, Margolis EB. Ventral tegmental area: cellular heterogeneity, connectivity
851 and behaviour. *Nat. Rev. Neurosci.* 2017, **18**(2)**:** 73.
852 48. Cohen JY, Haesler S, Vong L, Lowell BB, Uchida N. Neuron-type-specific signals
853 for reward and punishment in the ventral tegmental area. *Nature* 2012, **482**(7383)**:** 85-
854 88.
855 49. Gunaydin L A, Grosenick L, Finkelstein J C, Kauvar I V, Fenno L E, Adhikari A*, et*
856 *al.* Natural Neural Projection Dynamics Underlying Social Behavior. *Cell* 2014,
857 **157**(7)**:** 1535-1551.
858 50. Yu Q, Teixeira CM, Mahadevia D, Huang Y, Balsam D, Mann J J*, et al.* Dopamine
859 and serotonin signaling during two sensitive developmental periods differentially
860 impact adult aggressive and affective behaviors in mice. *Mol. Psychiatry* 2014, **19**(6)**:**
861 688-698.
862 51. Yang Y, Wu M, Vázquez-Guardado A, Wegener AJ, Grajales-Reyes JG, Deng Y*, et*
863 *al.* Wireless multilateral devices for optogenetic studies of individual and social
864 behaviors. *Nat. Neurosci.* 2021, **24**(7)**:** 1035-1045.
865 52. Al-Hasani R, McCall JG, Shin G, Gomez AM, Schmitz GP, Bernardi JM*, et al.*
866 Distinct Subpopulations of Nucleus Accumbens Dynorphin Neurons Drive Aversion
867 and Reward. *Neuron* 2015, **87**(5)**:** 1063-1077.

868 53. Sun F, Zeng J, Jing M, Zhou J, Feng J, Owen SF, *et al.* A Genetically Encoded
869 Fluorescent Sensor Enables Rapid and Specific Detection of Dopamine in Flies, Fish,
870 and Mice. *Cell* 2018, **174**(2)**:** 481-496 e419.
871 54. Yuan L, Dou YN, Sun YG. Topography of Reward and Aversion Encoding in the
872 Mesolimbic Dopaminergic System. *J. Neurosci.* 2019, **39**(33)**:** 6472-6481.
873 55. Sun F, Zhou J, Dai B, Qian T, Zeng J, Li X, *et al.* Next-generation GRAB sensors for
874 monitoring dopaminergic activity in vivo. *Nat. Methods* 2020, **17**(11)**:** 1156-1166.
875 56. Lin R, Liang J, Wang R, Yan T, Zhou Y, Liu Y, *et al.* The Raphe Dopamine System
876 Controls the Expression of Incentive Memory. *Neuron* 2020, **106**(3)**:** 498-514.e498.
877 57. Cui G, Jun SB, Jin X, Pham MD, Vogel SS, Lovinger DM, *et al.* Concurrent
878 activation of striatal direct and indirect pathways during action initiation. *Nature*
879 2013, **494**(7436)**:** 238-242.
880 58. Yuan L, Liang T-Y, Deng J, Sun Y-G. Dynamics and functional role of dopaminergic
881 neurons in the ventral tegmental area during itch processing. *J. Neurosci.* 2018,
882 **38**(46)**:** 9856-9869.
883 59. Li Y, Li C-Y, Xi W, Jin S, Wu Z-H, Jiang P, *et al.* Rostral and caudal ventral
884 tegmental area GABAergic inputs to different dorsal raphe neurons participate in
885 opioid dependence. *Neuron* 2019, **101**(4)**:** 748-761.
886 60. Taylor NE, Van Dort CJ, Kenny JD, Pei J, Guidera JA, Vlasov KY, *et al.* Optogenetic
887 activation of dopamine neurons in the ventral tegmental area induces reanimation
888 from general anesthesia. *Proc. Natl. Acad. Sci. U.S.A.* 2016, **113**(45)**:** 12826-12831.
889 61. Chang CY, Gardner M, Di Tillio MG, Schoenbaum G. Optogenetic blockade of
890 dopamine transients prevents learning induced by changes in reward features. *Curr.*
891 *Biol.* 2017, **27**(22)**:** 3480-3486.

892 62. de Chaumont F, Ey E, Torquet N, Lagache T, Dallongeville S, Imbert A*, et al.* Real-
893 time analysis of the behaviour of groups of mice via a depth-sensing camera and
894 machine learning. *Nat. Biomed. Eng.* 2019, **3**(11)**:** 930-942.
895 63. Kingsbury L, Huang S, Raam T, Letizia SY, Wei D, Hu RK*, et al.* Cortical
896 representations of conspecific sex shape social behavior. *Neuron* 2020, **107**(5)**:** 941-
897 953.
898 64. Kingsbury L, Huang S, Wang J, Gu K, Golshani P, Wu YE*, et al.* Correlated neural
899 activity and encoding of behavior across brains of socially interacting animals. *Cell*
900 2019, **178**(2)**:** 429-446.
901 65. Hong W, Kim D-W, Anderson DJ. Antagonistic control of social versus repetitive
902 self-grooming behaviors by separable amygdala neuronal subsets. *Cell* 2014, **158**(6)**:**
903 1348-1361.
904 66. Chiang C-H, Won SM, Orsborn AL, Yu KJ, Trumpis M, Bent B*, et al.* Development
905 of a neural interface for high-definition, long-term recording in rodents and nonhuman
906 primates. *Sci. Transl. Med.* 2020, **12**(538)**:** eaay4682.
907 67. Qazi R, Gomez AM, Castro DC, Zou Z, Sim JY, Xiong Y*, et al.* Wireless optofluidic
908 brain probes for chronic neuropharmacology and photostimulation. *Nat. Biomed. Eng.*
909 2019, **3**(8)**:** 655-669.
910 68. Lu L, Gutruf P, Xia L, Bhatti DL, Wang X, Vazquez-Guardado A*, et al.* Wireless
911 optoelectronic photometers for monitoring neuronal dynamics in the deep brain. *Proc.*
912 *Natl. Acad. Sci. U.S.A.* 2018, **115**(7)**:** E1374-E1383.
913 69. Liu C, Zhao Y, Cai X, Xie Y, Wang T, Cheng D*, et al.* A wireless, implantable
914 optoelectrochemical probe for optogenetic stimulation and dopamine detection.
915 *Microsyst. Nanoeng.* 2020, **6**(1)**:** 1-12.

916 70. Vierock J, Rodriguez-Rozada S, Dieter A, Pieper F, Sims R, Tenedini F*, et al.*
917 BiPOLES is an optogenetic tool developed for bidirectional dual-color control of
918 neurons. *Nat. Commun.* 2021, **12**(1)**:** 4527.
919 71. Lin J Y, Knutsen P M, Muller A, et al. ReaChR: a red-shifted variant of
920 channelrhodopsin enables deep transcranial optogenetic excitation. *Nat. Neurosci.*
921 2013, **16**(10): 1499-1508.
922 72. Chen R, Gore F, Nguyen Q-A, Ramakrishnan C, Patel S, Kim SH, et al. Deep brain
923 optogenetics without intracranial surgery. *Nat. Biotechnol.* 2021, **39**(2): 161-164.
924 73. Selimbeyoglu A, Kim CK, Inoue M, Lee SY, Hong ASO, Kauvar I*, et al.* Modulation
925 of prefrontal cortex excitation/inhibition balance rescues social behavior in
926 CNTNAP2-deficient mice. *Sci. Transl. Med.* 2017, **9**(401)**:** eaah6733.
927 74. Kravitz AV, Freeze BS, Parker PRL, Kay K, Thwin MT, Deisseroth K*, et al.*
928 Regulation of parkinsonian motor behaviours by optogenetic control of basal ganglia
929 circuitry. *Nature* 2010, **466**(7306)**:** 622-626.
930 75. Keppeler D, Schwaerzle M, Harczos T, Jablonski L, Dieter A, Wolf B*, et al.*
931 Multichannel optogenetic stimulation of the auditory pathway using microfabricated
932 LED cochlear implants in rodents. *Sci. Transl. Med.* 2020, **12**(553)**:** eabb8086.
933 76. Michoud F, Seehus C, Schönle P, Brun N, Taub D, Zhang Z*, et al.* Epineural
934 optogenetic activation of nociceptors initiates and amplifies inflammation. *Nat.*
935 *Biotechnol.* 2021, **39**(2)**:** 179-185.
936 77. Kathe C, Michoud F, Schönle P, Rowald A, Brun N, Ravier J*, et al.* Wireless closed-
937 loop optogenetics across the entire dorsoventral spinal cord in mice. *Nat. Biotechnol.*
938 2021: 1-11.

939 78. Gebhart SC, Lin WC, Mahadevan-Jansen A. In vitro determination of normal and
940 neoplastic human brain tissue optical properties using inverse adding-doubling. *Phys.*
941 *Med. Biol.* 2006, **51**(8)**:** 2011-2027.
942 79. Peirson SN, Brown LA, Pothecary CA, Benson LA, Fisk AS. Light and the laboratory
943 mouse. *J. Neurosci. Methods* 2018, **300:** 26-36.
944 80. Lu L, Wang R, Luo M. An optical brain-to-brain interface supports rapid information
945 transmission for precise locomotion control. *Sci China Life Sci* 2020, **63**(6)**:** 875-885.
946 81. Wu X, Dong X, Wu Z, Cao H, Niu D, Qu J*, et al.* A novel method for purification of
947 recombinant adenoassociated virus vectors on a large scale. *Sci. Bull.* 2001, **46**(6)**:**
948 485-488.
949 82. Liu Z, Zhou J, Li Y, Hu F, Lu Y, Ma M*, et al.* Dorsal raphe neurons signal reward
950 through 5-HT and glutamate. *Neuron* 2014, **81**(6)**:** 1360-1374.

Acknowledgements

This work is supported by National Natural Science Foundation of China (NSFC) (61874064), Beijing Municipal Natural Science Foundation (4202032), Tsinghua University Initiative Scientific Research Program, Center for Flexible Electronics Technology at Tsinghua University, Beijing National Research Center for Information Science and Technology (BNR2019ZS01005), CAS Key Laboratory of Brain Connectome and Manipulation (Lab No.2019DP173024, Project No.KFKT2020006). We thank Prof. Y. Li (Peking University) for support on $GRAB_{DA2m}$, Y. Zhou and Y. Ju (Chinese Institute for Brain Research, Beijing) for support on stGtACR2.

Author contributions

X. S. and M. L. developed the concepts. L. Li, G. T., Y. Z., X. C., Z. S., H. D., C. L., Y. X., H. W., L. Y. and X. S. performed material, device and circuit design, fabrication and characterization. L. Li, X. C., D. C, and X. S. performed the simulations. L. Li, L. Lu, Y. R., G. T., X. F., L. Y., M. L., and X. S. designed and performed biological experiments. L. Li, L. Lu, M. L. and X. S. wrote the paper in consultation with other authors.

Competing interests

The authors declare no competing interests.

Data and materials availability

All data needed to evaluate the conclusions in the paper are present in the paper and/or the Supplementary information.

Figure 1

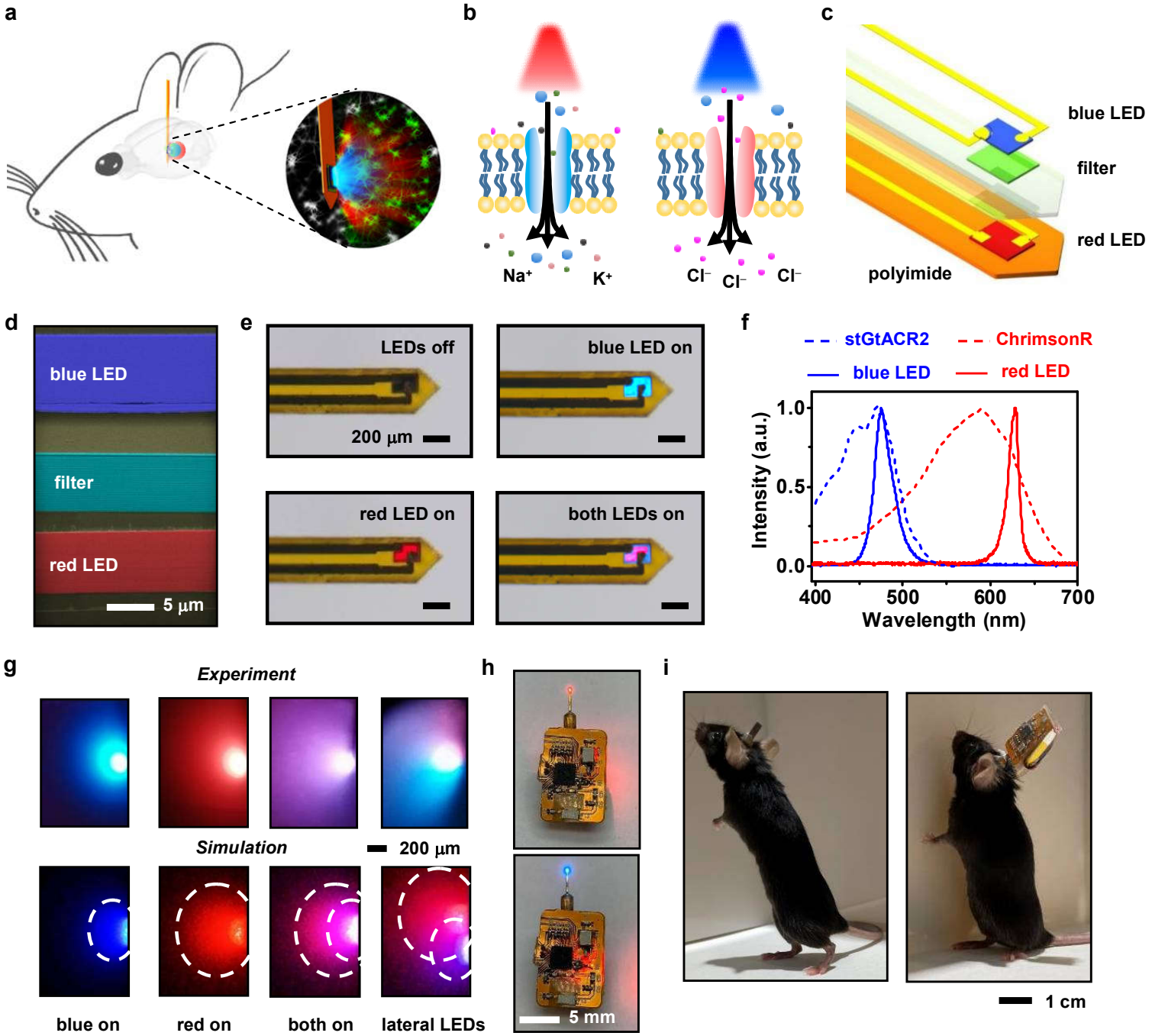
a
b
Na+
K+
Cl−
Cl−
Cl−
c
blue LED
filter
red LED
polyimide
d
blue LED
filter
red LED
5 µm
e
LEDs off
200 µm
blue LED on
red LED on
both LEDs on
f
stGtACR2
ChrimsonR
blue LED
red LED
Intensity (a.u.)
1.0
0.5
0.0
400
500
600
700
Wavelength (nm)
g
Experiment
Simulation
200 µm
blue on
red on
both on
lateral LEDs
h
5 mm
i
1 cm

Figure 1. Wirelessly operated, dual-color microscale LED (micro-LED) probes for bidirectional, colocalized optogenetic control of neural activities. a, Schematic view of the probe inserted into the target brain area to perform dual-color neural activation and inhibition. **b**, Schematic, cellular scale depiction of the modulation function: red light regulates the cation channel ChrimsonR for depolarization, while blue light regulates the anion channel stGtACR2 for hyperpolarization. **c**, Exploded view of the dual-color LED probe made from vertically stacked blue and red thin-film micro-LEDs assembled on a flexible polyimide (PI) substrate, with a thin-film filter interface for spectrally selective reflection and transmission. **d**, Cross-sectional scanning electron microscopic (SEM) image of the probe structure, with false colors highlighting (from bottom to top) the indium gallium arsenide (InGaP) red micro-LED, the multilayer silicon dioxide / titanium dioxide (SiO_2/TiO_2) filter, and the indium gallium nitride (InGaN) blue micro-LED. Layers of SU-8 photoresists serve as the bonding materials. **e**, Optical images of a micro-LED probe (with a thickness of ~120 μm and a width of ~320 μm), showing independent control of blue and red emissions under current injections. **f**, Emission spectra of the blue and red micro-LEDs, in comparison with the action spectra of ion channels stGtACR2 and ChrimsonR. **g**, Experimental photographs and simulated results illustrating blue and red light propagations for a micro-LED probe embedded into a brain phantom (column 1–3). Results for a probe with laterally assemble blue and red LEDs are also presented (column 4), showing misplaced blue and red emissions. Iso-intensity lines show 10% of the maximum power. **h**, Images of a micro-LED probe integrated with a wireless circuit for independent control of dual-color emissions. **i**, Photos of a behaving mouse after intracranial implantation of a probe, with (right) and without (left) the wireless circuit module.

Figure 2

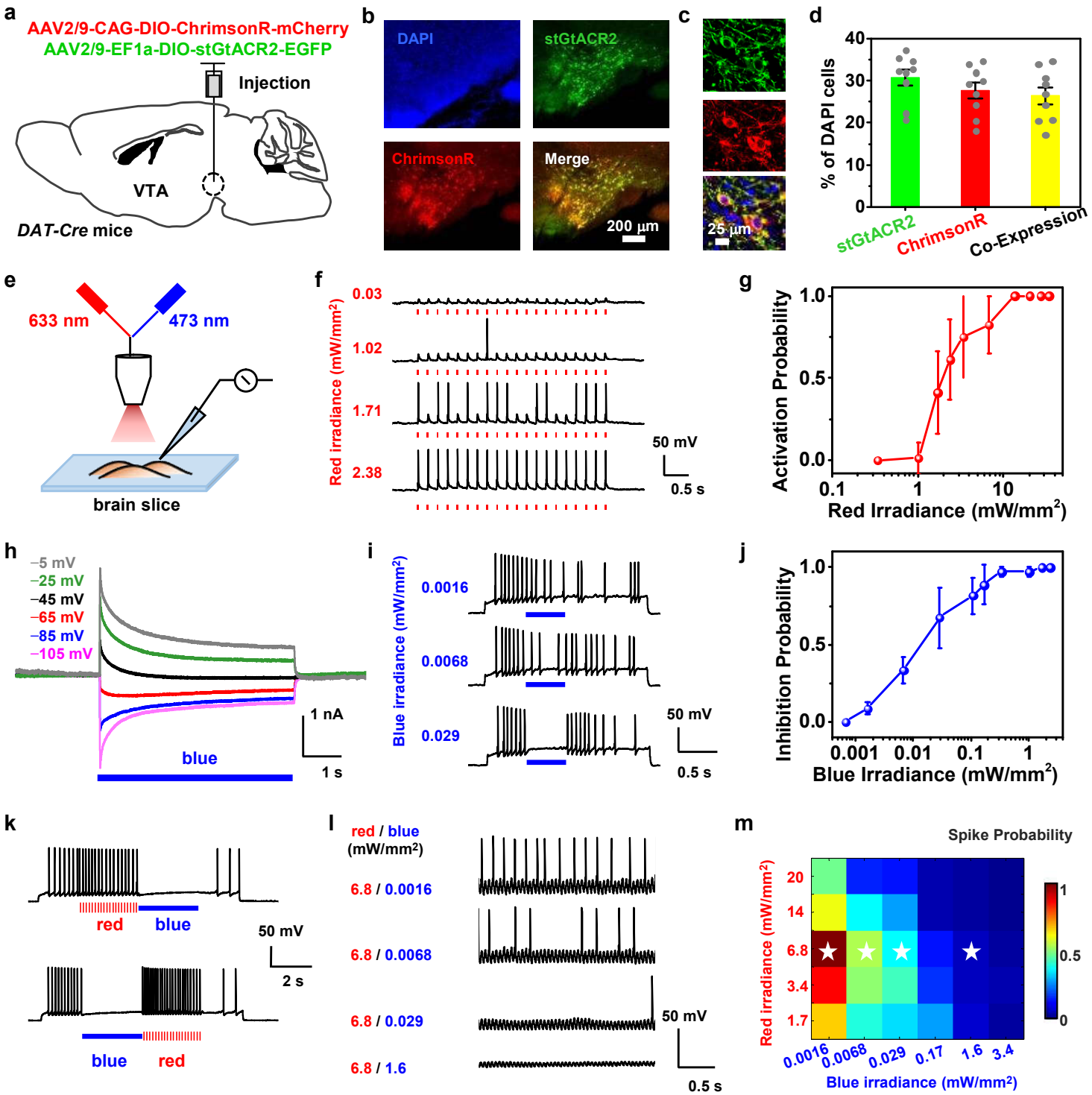
a
AAV2/9-CAG-DIO-ChrimsonR-mCherry
AAV2/9-EF1a-DIO-stGtACR2-EGFP
Injection
VTA
DAT-Cre mice
b
DAPI
stGtACR2
ChrimsonR
Merge
200 µm
c
25 µm
d
% of DAPI cells
40
30
20
10
0
stGtACR2
ChrimsonR
Co-Expression
e
633 nm
473 nm
brain slice
f
Red irradiance (mW/mm²)
0.03
1.02
1.71
2.38
50 mV
0.5 s
g
Activation Probability
1.0
0.5
0.0
0.1
1
10
Red Irradiance (mW/mm²)
h
−5 mV
−25 mV
−45 mV
−65 mV
−85 mV
−105 mV
1 nA
1 s
blue
i
Blue irradiance (mW/mm²)
0.0016
0.0068
0.029
50 mV
0.5 s
j
Inhibition Probability
1.0
0.5
0.0
0.001
0.01
0.1
1
Blue Irradiance (mW/mm²)
k
red
blue
50 mV
2 s
blue
red
l
red / blue
(mW/mm²)
6.8 / 0.0016
6.8 / 0.0068
6.8 / 0.029
6.8 / 1.6
50 mV
0.5 s
m
Spike Probability
Red irradiance (mW/mm²)
20
14
6.8
3.4
1.7
0.0016
0.0068
0.029
0.17
1.6
3.4
Blue irradiance (mW/mm²)
1
0.5
0

Figure 2. Bidirectional optogenetic activation and inhibition of neurons with red and blue light stimulation. a, Schematic strategy for co-expressing ChrimsonR and stGtACR2 in the ventral tegmental area (VTA) of *DAT-cre* mice. **b**, Immunostained fluorescence images of the VTA region expressing DAPI (blue), stGtACR2 (green), and ChrimsonR (red) and a merged image, 3 weeks after viral injection. **c**, Zoomed view showing cells co-expressing stGtACR2 (green) and ChrimsonR (red). **d**, Percentages of stGtACR2-, ChrimsonR- and co-expressing neurons among DAPI cells in the VTA (mean ± s.e.m., 3 slices per mouse, n = 3 mice). **e**, Illustration of the experiment setup with combined blue (480 nm) and red (633 nm) laser beams (spot diameter ~1 mm) for optogenetic stimulating brain slices during patch-clamp recordings *in vitro*. **f**, Example traces showing neural activation by pulsed red light at different irradiances (20 Hz, 10-ms pulse, 20-pulse train). **g**, Activated spike probability as a function of red irradiances (mean ± s.e.m., n = 4 cells). **h**, Example photocurrents of neurons at membrane potentials varied from −105 mV to −5 mV (bottom to top), under continuous blue light illumination (duration 5 s, irradiance 8 mW/mm^2). **i**, Example traces of neural inhibition by continuous blue light at different irradiances (duration 0.5 s). **j**, Inhibited spike probability as a function of blue irradiances (mean ± s.e.m., n = 5 cells). **k**, Traces presenting bidirectional spike activation and inhibition with alternating red and blue illuminations (Patching current +90 pA; Red: duration 3 s, 20 Hz, 10-ms pulse, 2.2 mW/mm^2; Blue: duration 3 s, 8.5 mW/mm^2). **l**, Example traces of neural activities with simultaneous red and blue illuminations at different irradiances (duration 6 s). **m**, Summarized plot of measured spike probability (normalized mean values) as a function of red and blue irradiances (n = 5 cells). The stars indicate the position of the four example traces shown in Fig. 2l.

Figure 3

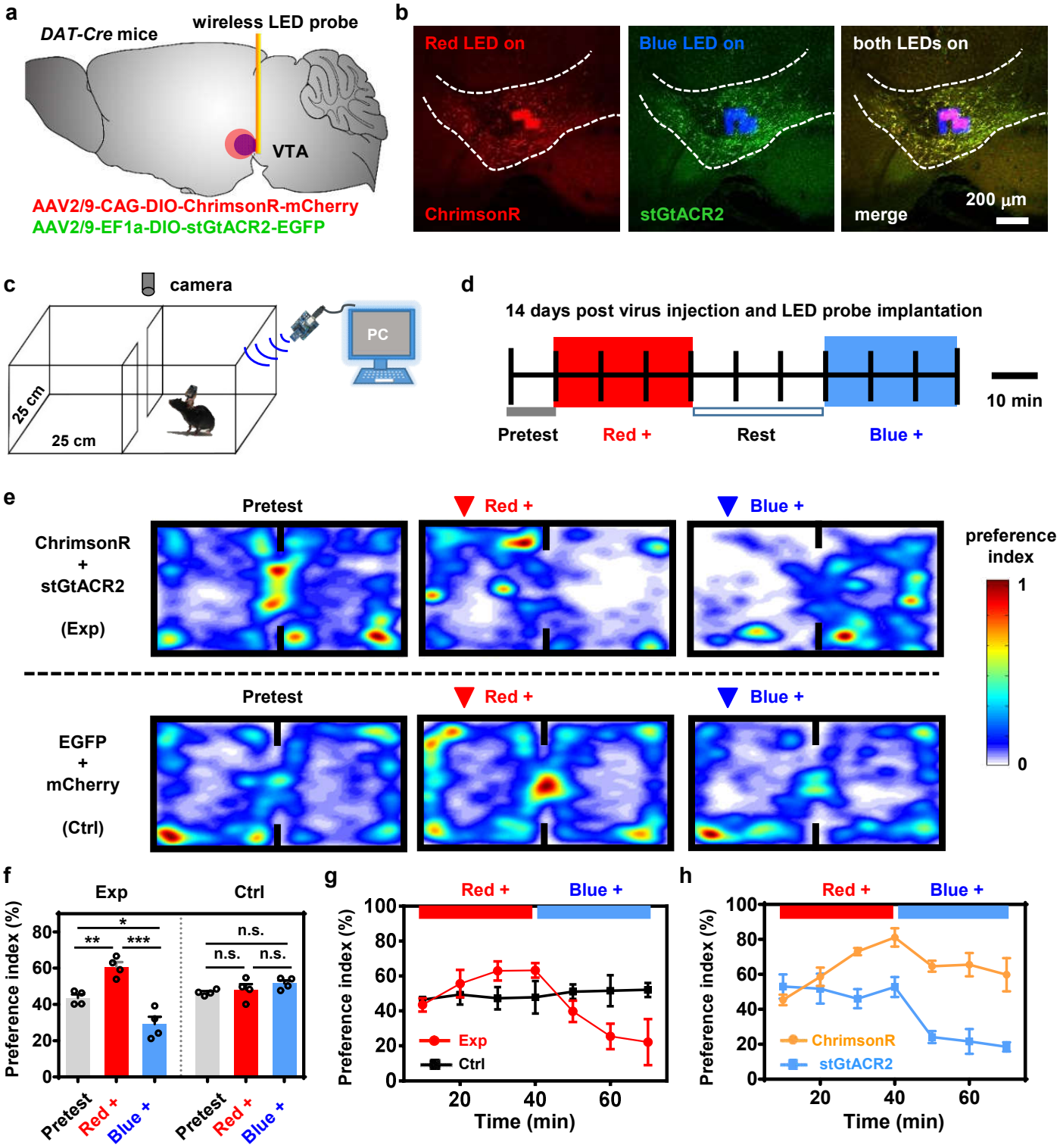
a
DAT-Cre mice
wireless LED probe
VTA
AAV2/9-CAG-DIO-ChrimsonR-mCherry
AAV2/9-EF1a-DIO-stGtACR2-EGFP
b
Red LED on
ChrimsonR
Blue LED on
stGtACR2
both LEDs on
merge
200 μm
c
camera
PC
25 cm
25 cm
d
14 days post virus injection and LED probe implantation
10 min
Pretest
Red +
Rest
Blue +
e
Pretest
Red +
Blue +
ChrimsonR
+
stGtACR2
(Exp)
EGFP
+
mCherry
(Ctrl)
preference
index
1
0
f
Exp
Ctrl
Preference index (%)
n.s.
Pretest
Red +
Blue +
g
Red +
Blue +
Preference index (%)
Exp
Ctrl
Time (min)
h
Red +
Blue +
Preference index (%)
ChrimsonR
stGtACR2
Time (min)

Figure 3. Bidirectional, *in vivo* optogenetic regulation of mice preference or aversion behaviors with wirelessly operated, dual-color microscale LED (micro-LED) probes. a, Diagram illustrating the combined viral injection (AAV2/9-CAG-DIO-ChrimsonR-mCherry and AAV2/9-EF1a-DIO-stGtACR2-EGFP) followed by implanting the micro-LED probe into the VTA of *DAT-cre* mice. **b**, Micrographs of the VTA showing co-expression of stGtACR2 and ChrimsonR, with a dual-color micro-LED probe embedded into the tissue. **c**, Illustration of the real-time place preference test with a two-compartment arena, where a mouse receives signals for dual-color control and its locomotion is recorded by a camera. **d**, Patterns used for optogenetic modulations, including a 10-min pretest, a 30-min red LED stimulation (20 Hz, 10-ms pulse, current 7 mA), a 30-min rest, and a 30-min blue LED stimulation (continuous, current 5 mA). **e**, Representative heat maps showing real-time preference and aversion behavior following red or blue stimulation for mice co-expressing stGtACR2 + ChrimsonR (experiment, or Exp) or EGFP + mCherry (control, or Ctrl). **f**, Summary of preference indices (the ratio of the time that mice spend in the left chamber to the whole recorded time) under red and blue stimulations for Exp and Ctrl groups (n = 4 mice each). Student's t test, * $P < 0.05$, ** $P < 0.01$, *** $P < 0.001$, n.s. $P > 0.05$. **g**, Preference indices measured at different times under red and blue stimulations for Exp and Ctrl groups (n = 4 mice each). **h**, Preference indices measured at different times under red and blue stimulations for groups expressing only ChrimsonR or stGtACR2 (n = 3 mice each).

Figure 4

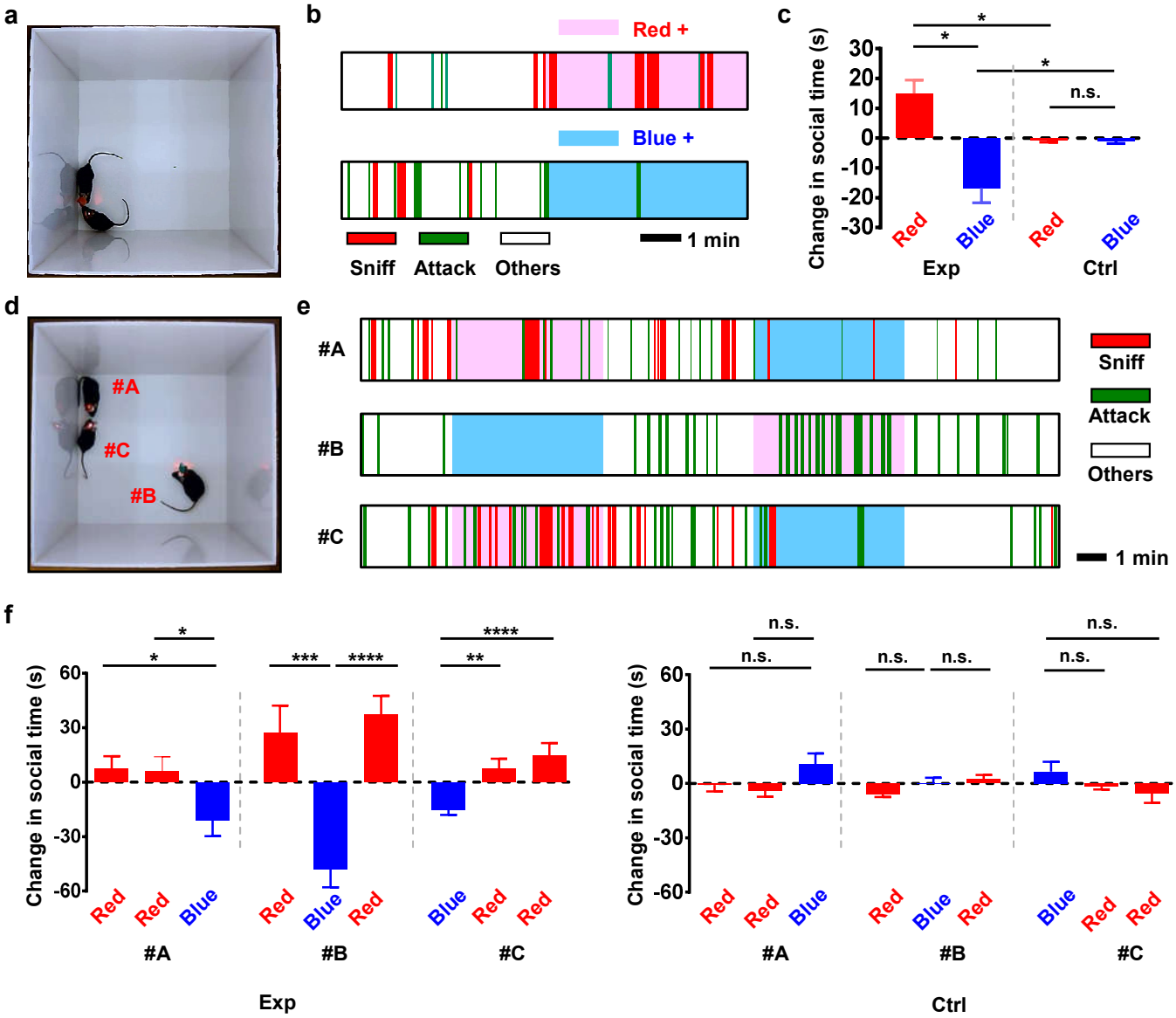
a
b
Red +
Blue +
Sniff
Attack
Others
1 min
c
Change in social time (s)
30
20
10
0
-10
-20
-30
*
*
*
n.s.
Red
Blue
Red
Blue
Exp
Ctrl
d
#A
#C
#B
e
#A
#B
#C
Sniff
Attack
Others
1 min
f
Change in social time (s)
60
30
0
-30
-60
*
*
***
****
****
**
Red
Red
Blue
Red
Blue
Red
Blue
Red
Red
#A
#B
#C
Exp
n.s.
n.s.
n.s.
n.s.
n.s.
n.s.
Red
Red
Blue
Red
Blue
Red
Blue
Red
Red
#A
#B
#C
Ctrl

Figure 4. Bidirectional, *in vivo* optogenetic control of mice social interactions with wirelessly operated, dual-color micro-LED probes. a, Photograph of two *DAT-cre* mice with wireless probes in an arena (30×30 cm^2). Experiment groups (Exp) express stGtACR2 + ChrimsonR, and control groups (Ctrl) express EGFP + mCherry. **b,** Representative behavioral sequences recorded for one mouse receiving red or blue stimulations during social interactions. Here sniffing and attacking behaviors are highlighted and labeled, and other behaviors include locomotion, resting and escaping. **c,** Summary of changes in social interactions under red or blue stimulations. Here we compare the time spent in sniff and attack during the 5 mins light stimulation with the 5 mins resting state. $n = 4$ groups for both Exp and Ctrl. **d,** Photograph of three *DAT-cre* mice with wireless probes in an arena. **e,** Representative behavioral sequences recorded for the three mice (#A, #B, #C) receiving red or blue stimulation during social interactions. **f,** Summary of changes in social interactions under red or blue stimulations for each mouse. $n = 4$ groups for both Exp (left) and Ctrl (right). All data are represented as mean ± s.e.m.. Student's *t* test, * $P < 0.05$, ** $P < 0.01$, *** $P < 0.001$, **** $P < 0.0001$, n.s. $P > 0.05$.

Figure 5

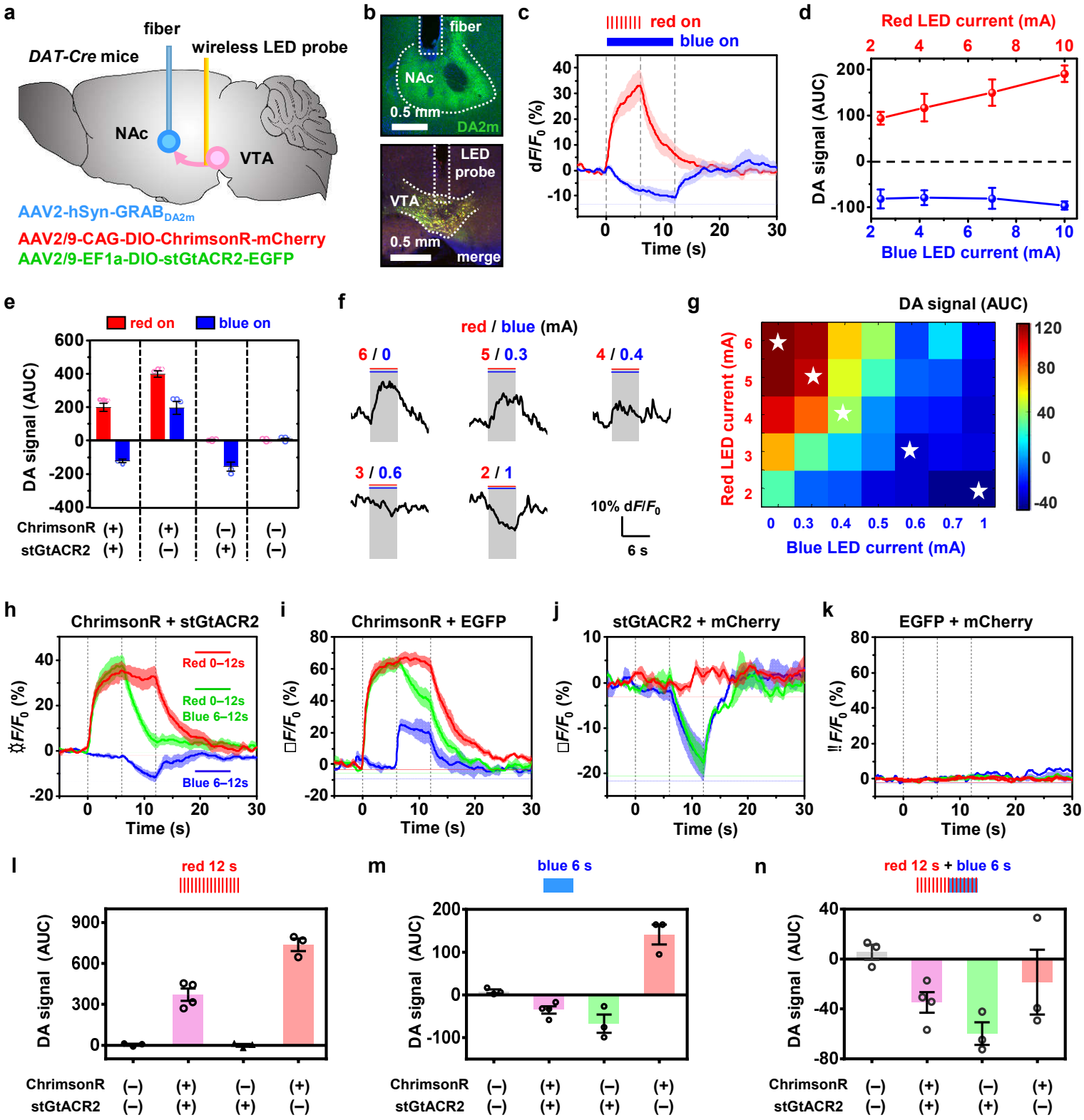
a
fiber
wireless LED probe
DAT-Cre mice
NAc
VTA
AAV2-hSyn-GRAB$_{DA2m}$
AAV2/9-CAG-DIO-ChrimsonR-mCherry
AAV2/9-EF1a-DIO-stGtACR2-EGFP
b
fiber
NAc
0.5 mm
DA2m
LED probe
VTA
0.5 mm
merge
c
red on
blue on
dF/F0 (%)
Time (s)
d
Red LED current (mA)
DA signal (AUC)
Blue LED current (mA)
e
red on
blue on
DA signal (AUC)
ChrimsonR
stGtACR2
f
red / blue (mA)
6 / 0
5 / 0.3
4 / 0.4
3 / 0.6
2 / 1
10% dF/F0
6 s
g
DA signal (AUC)
Red LED current (mA)
Blue LED current (mA)
h
ChrimsonR + stGtACR2
Red 0–12s
Red 0–12s
Blue 6–12s
Blue 6–12s
Time (s)
i
ChrimsonR + EGFP
Time (s)
j
stGtACR2 + mCherry
Time (s)
k
EGFP + mCherry
Time (s)
l
red 12 s
DA signal (AUC)
ChrimsonR
stGtACR2
m
blue 6 s
DA signal (AUC)
ChrimsonR
stGtACR2
n
red 12 s + blue 6 s
DA signal (AUC)
ChrimsonR
stGtACR2

Figure 5. Bidirectional, *in vivo* optogenetic control of dopamine (DA) release simultaneously recorded in the nucleus accumbens (NAc) during dual-color stimulation in the VTA. a, Diagram illustrating the combined viral injection (AAV2/9-CAG-DIO-ChrimsonR-mCherry and AAV2/9-EF1a-DIO-stGtACR2-EGFP) followed by implanting the micro-LED probe into the VTA, and the viral injection (AAV2-hSyn-GRAB$_{DA2m}$) followed by optical fiber implantation into the NAc of *DAT-cre* mice. **b**, Micrographs of (top) the NAc showing expression of DA2m and the fiber track, (bottom) the VTA showing co-expression of stGtACR2 and ChrimsonR (merged color) and the micro-LED probe track, 2 weeks after viral injection and probe implantation. **c**, Representative traces of DA signals in response to stimulations by the red LED (7 mA, 20 Hz, 20-ms pulse, 6 s) and the blue LED (2.4 mA, continuous, 12 s). The solid lines and shaded areas indicate the mean and s.e.m., respectively (n = 4 mice). **d**, Accumulative DA signals in response to red and blue stimulations under different LED currents. AUC: area under the curve during stimulation. **e**, Summary of measured DA signals (AUC) in response to red or blue stimulations (Red LED: 20 Hz, 20-ms pulse, 10 mA, 6 s; Blue LED, continuous, 3 mA, 12 s) for different mouse groups expressing ChrimsonR + stGtACR2 (n = 4 mice), ChrimsonR + EGFP (n = 3 mice), stGtACR2 + mCherry (n = 3 mice), EGFP + mCherry (n = 3 mice). Student's t test. **f**, Example traces of DA signals under combined red and blue stimulations with varied LED currents. **g**, Summarized plot of measured DA signals (AUC) (mean value) as a function of red and blue LED currents for 6 s (n = 3 mice). The stars indicate results for five traces shown in Fig. 5f. **h–k**, Plots of optogenetically evoked DA transients in response to different stimulation patterns (Red: red LED on, 20 Hz, 20-ms pulse, 10 mA, 0–12 s; Blue: blue LED on, continuous, 3 mA, 6–12 s; Green: red LED on 0–12 s and blue LED on 6–12 s), for different mouse groups expressing different opsins. **h**, ChrimsonR + stGtACR2 (n = 4 mice). **i**, ChrimsonR + EGFP (n = 3 mice). **j**, stGtACR2 + mCherry (n = 3 mice). **k**, EGFP + mCherry (n = 3 mice). The solid lines and shaded areas indicate the mean and s.e.m., respectively. **l–n**, Summary of measured DA signals (AUC) for different mouse groups. **l**, red LED on, 20 Hz, 20-ms pulse, 10 mA, 0–12 s. **m**, blue LED on, continuous, 3 mA, 6–12 s. **n**, red LED on 0–12 s and blue LED on 6–12 s.

Figure S1

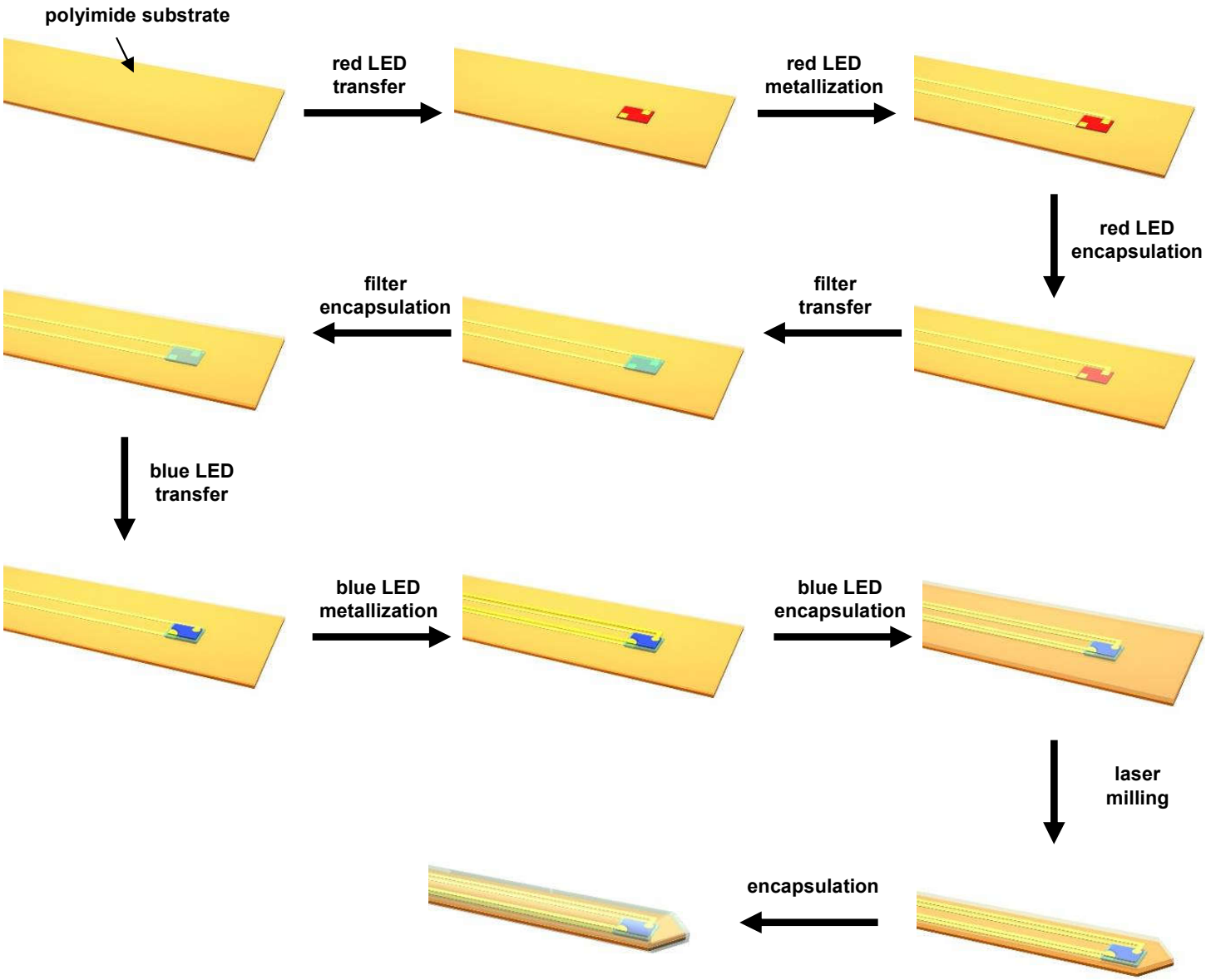

Figure S1. Schematic illustration of the process flow for fabricating the dual-color micro-LED probes, with vertically stacked red LED, filter and blue LED printed on PI substrates.

Figure S2

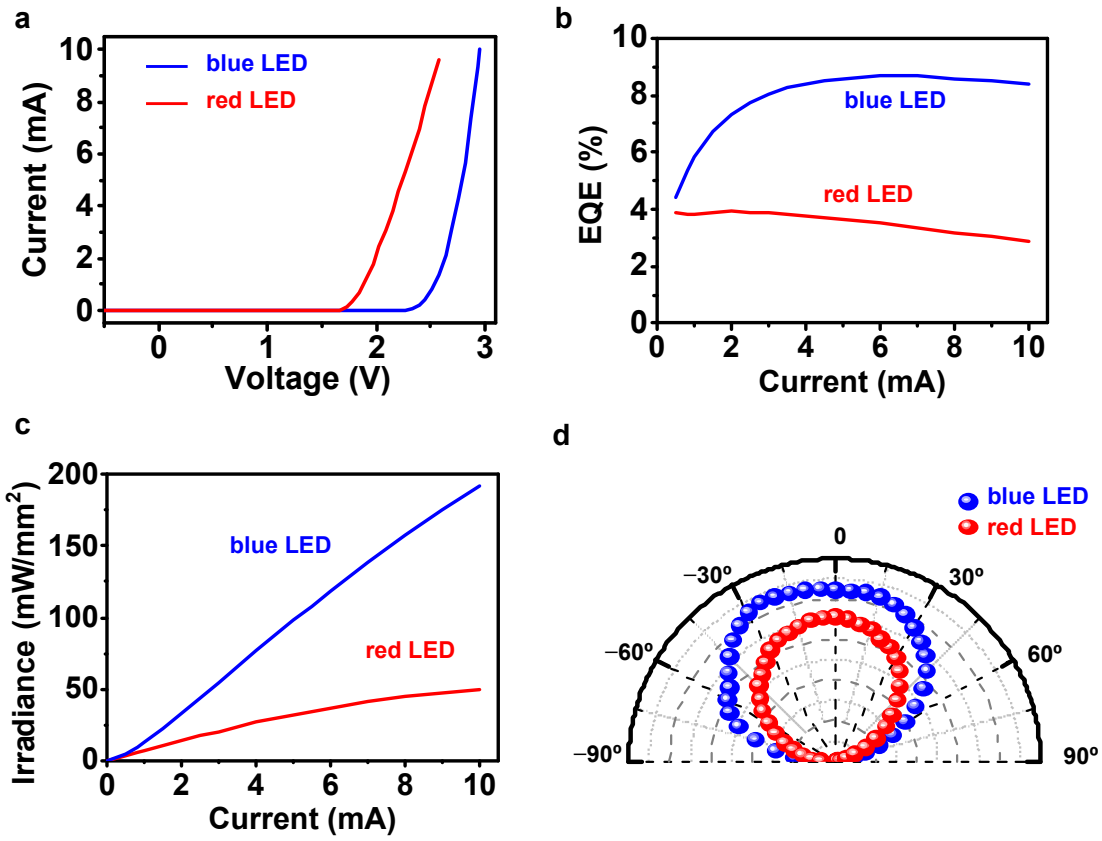

Figure S2. Measured optoelectronic properties of the red and the blue micro-LEDs in a probe structure. (a) Current–voltage curves. (b) External quantum efficiencies (EQEs) as a function of current. (c) Irradiance (power density on the LED surface) versus current. (d) Angular dependent emission profiles (in arbitrary unit).

Figure S3

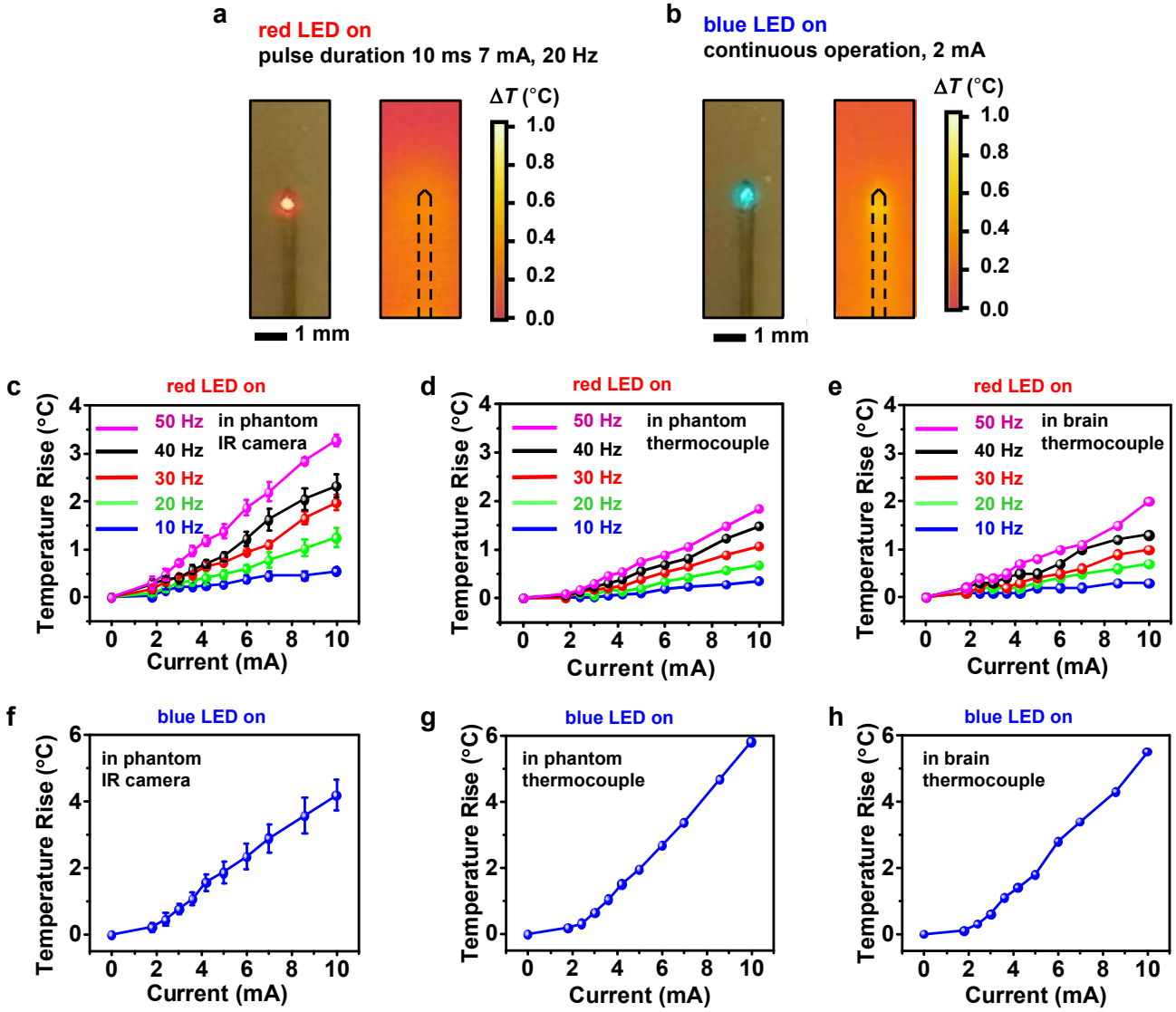

Figure S3. Measured thermal behaviors of a dual-color micro-LED probe. (a, b) Images and infrared (IR) thermographs showing a probe embedded into a brain phantom (~0.5 mm below the phantom surface). (a) Red LED on (injection current 7 mA, pulse frequency 20 Hz, pulse duration 10 ms). (b) Blue LED on (injection current 2 mA, continuous operation). (c) Measured temperature rise on the phantom surface by IR camera. (d) Measured temperature rise in the phantom by thermocouple. (e) Measured temperature rise in the brain of living mice by thermocouple. Red LED current 0–10 mA, frequency 10–50 Hz, pulse duration 10 ms). (f–h) Corresponding results when the blue LED is on (continuous mode).

Figure S4

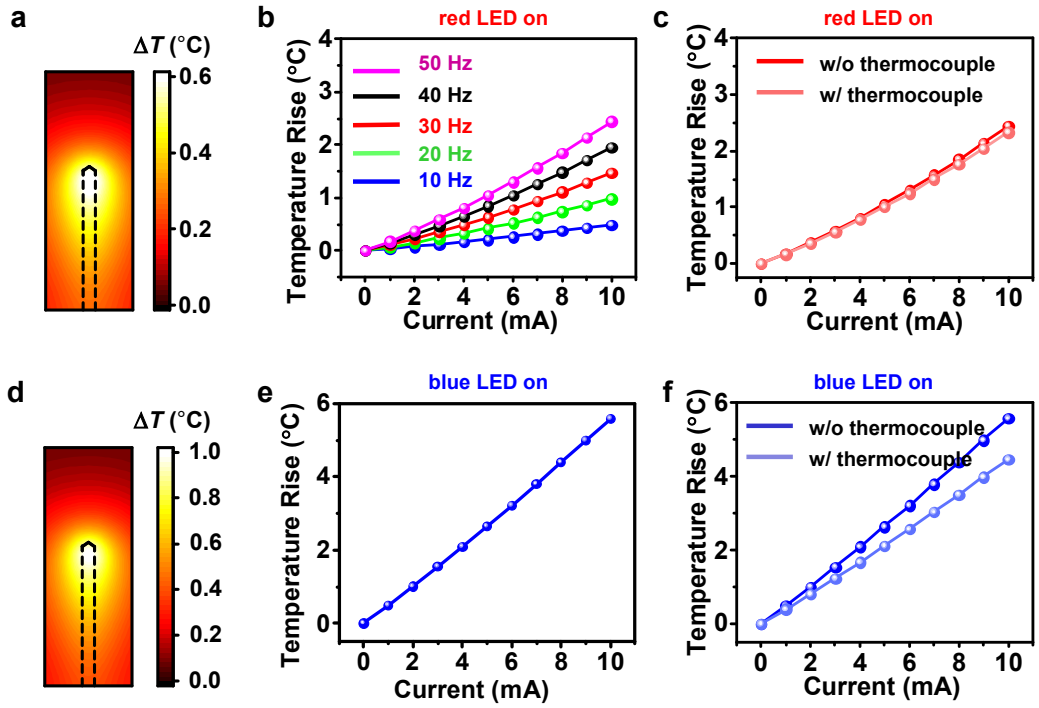

Figure S4. Simulated thermal behaviors of a dual-color micro-LED probe. (a) Simulated steady-state temperature distribution in the brain tissue surrounding the probe, when the red LED is on (current 7 mA, frequency 20 Hz, pulse duration 10 ms). (b) Simulated maximum temperature rise of the brain tissue when the red LED is in different operation conditions. (c) Simulated maximum temperature rise of the brain tissue when the red LED is on (frequency 50 Hz, pulse duration 10 ms). The results for models with and without the thermocouple are compared. (d–f) Corresponding results when the blue LED is on (continuous mode), current = 2 mA in (d).

Figure S5

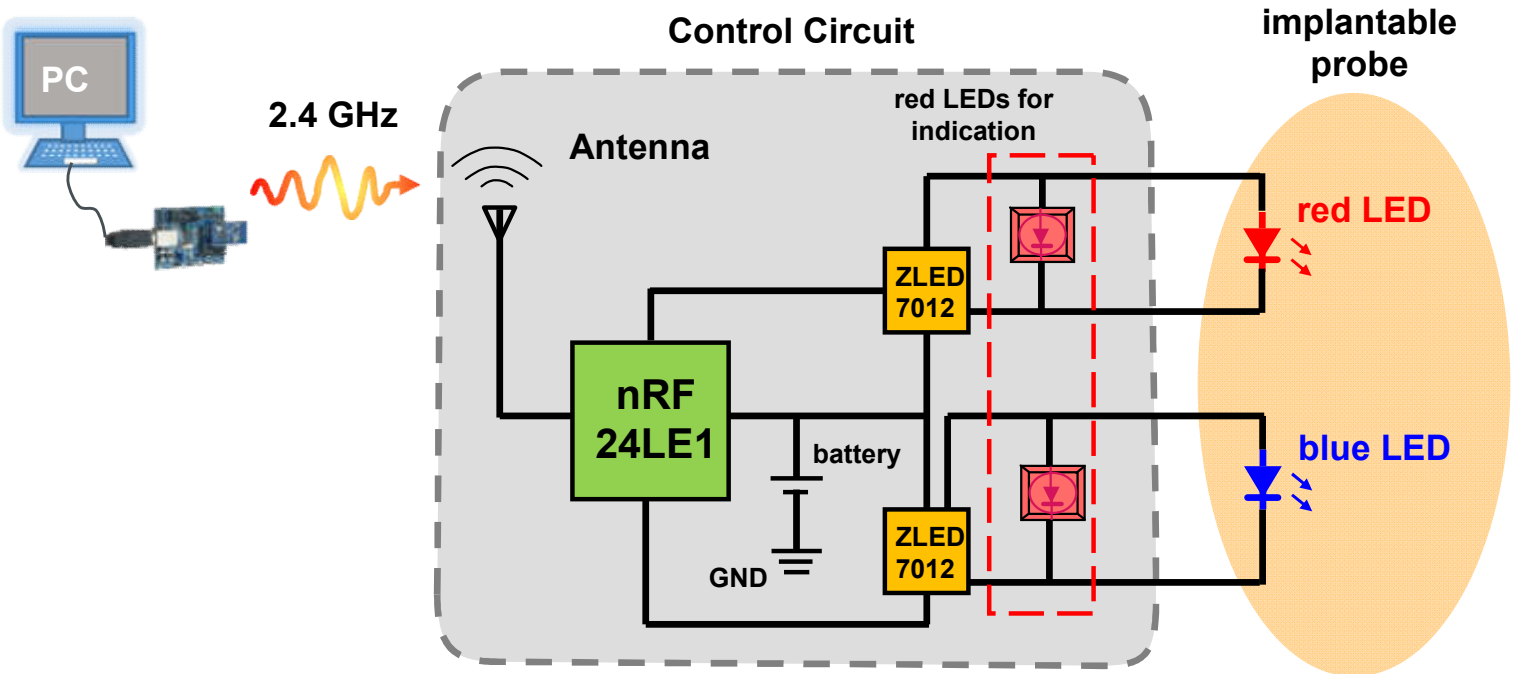

Figure S5. Schematic diagram showing the operational principle for the wireless circuit system controlling the dual-color micro-LED probe.

Figure S6

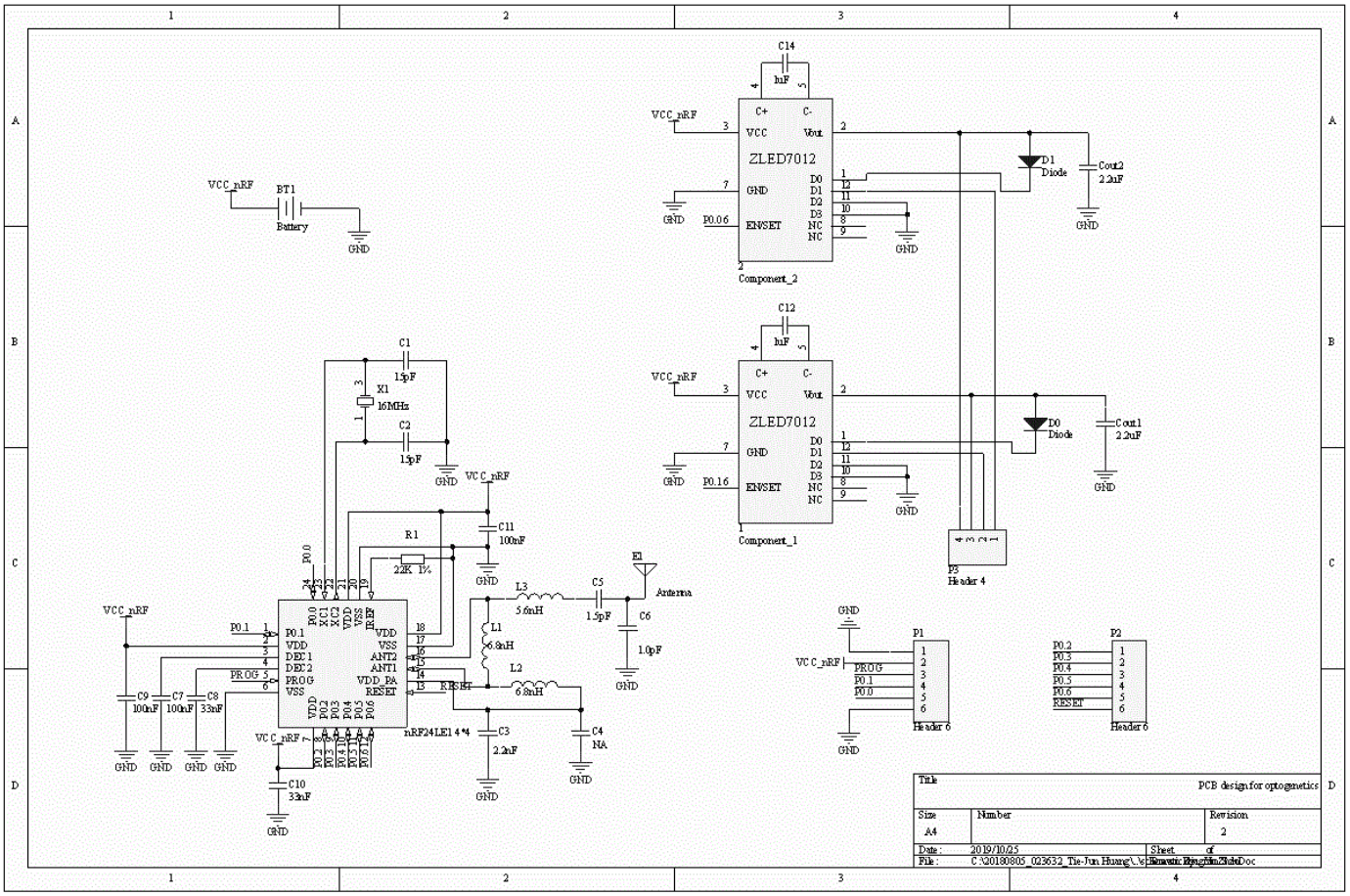

Figure S6. Detailed circuit design diagram of the wireless circuit system.

Figure S7

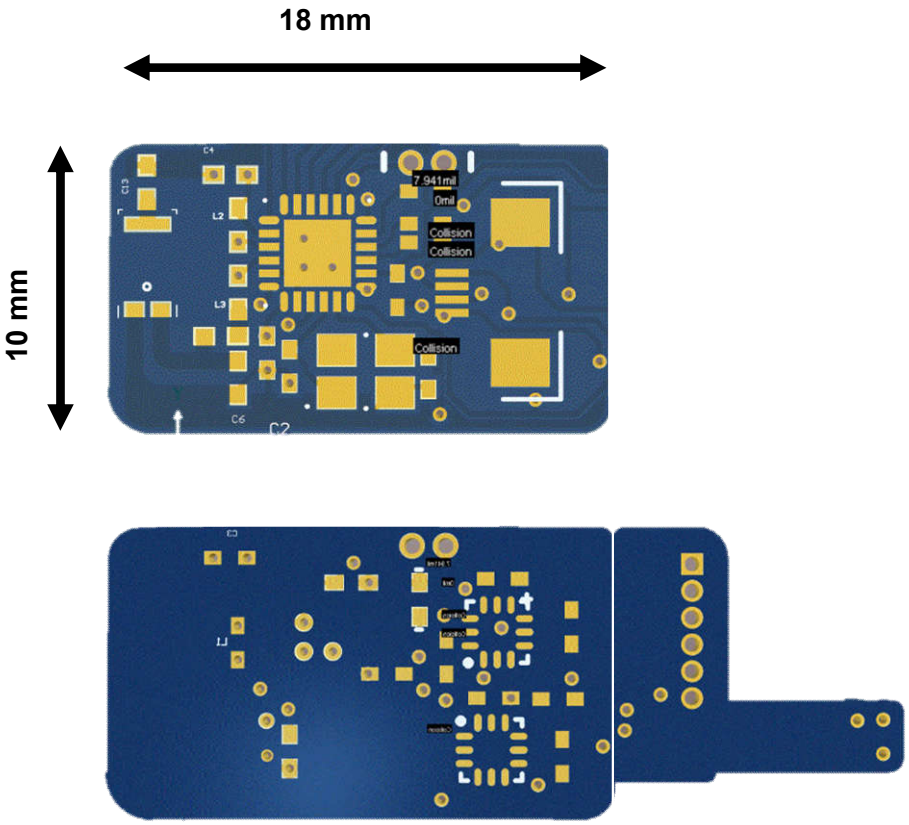

Figure S7. Layout of the designed printed circuit board (top: front view; bottom: back view).

Figure S8

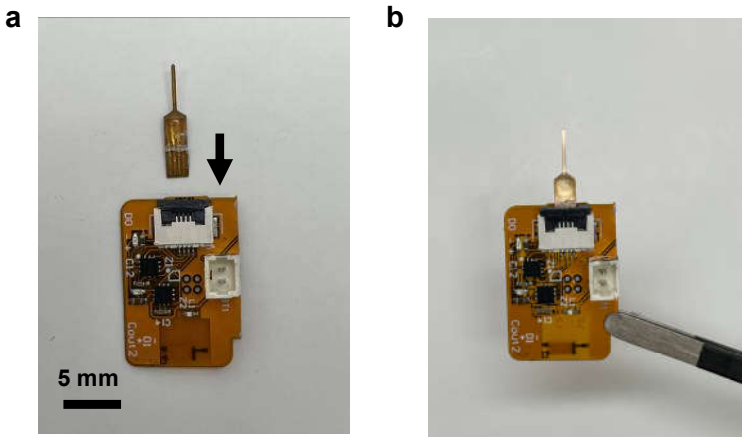

Figure S8. Optical images of a micro-LED probe and a control circuit (a) before and (b) after connection via a standard 4-pin connector.

Figure S9

	components
L1, L2	High frequency chip inductor +/- 5%, 6.8 nH
L3	High frequency chip inductor +/- 5%, 5.6 nH
C1, C2	NP0 +/- 2%, 15 pF
C3, C4	X7R +/- 10%, 2.2 nF
C5	NP0 +/- 0.1pF, 1.5 pF
C6	NP0 +/- 0.1pF, 1.0 pF
C7,C9,C11	X7R +/- 10%, 100 nF
C8,C10	X7R +/- 10%, 33 nF
C12,C14	X7R +/- 10%, 1 μF
Cout1,Cout2	2.2 μF
C13	NP0 50V, 10 pF
D0, D1	Indicating red LED, 610 nm, SMD 0402, 1 mm * 0.5 mm * 0.4 mm
R1	22 kΩ, 1%
nRF24LE1	nRF24LE1-F16Q24, QFN24 4 mm * 4 mm package, MCU
Component_1 Component_2	ZLED7012 ZI1R, LED current driver
X1	Crystal oscillator, SMD-3225, 16 MHz, CL=9 pF, +/- 60 ppm 3.2 mm * 2.5 mm package
E1	Antenna, H2U34WGTQW0100, AA055, 3.2 mm * 1.6 mm * 0.5 mm package
P1, P2	Pin Header, 6 pin, 1.25 mm, for programming
P3	FPC connector, 4 pin, 0.5 mm, for LED probe
P4	PCB header Connector, male, DIP Straight, 2 pin, 2.54 mm, for battery
Battery	Rechargeable lithium ion battery, 3.7 V, 45 mAh

Figure S9. List of components used in the wireless circuit system.

Figure S10

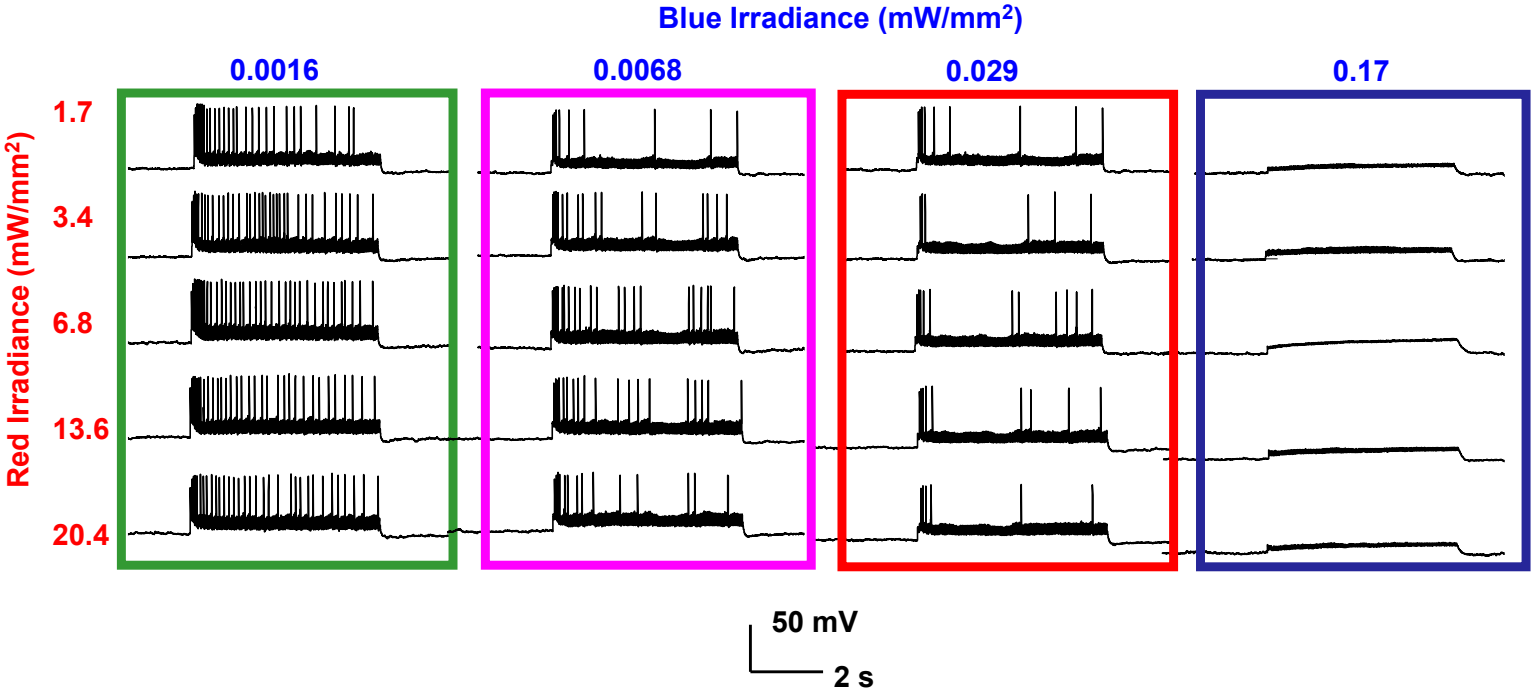

Figure S10. Recorded traces of a representative neuron with combined red and blue illumination at different irradiances. Red LED: 20 Hz, 10-ms pulse; Blue LED: continuous operation.

Figure S11

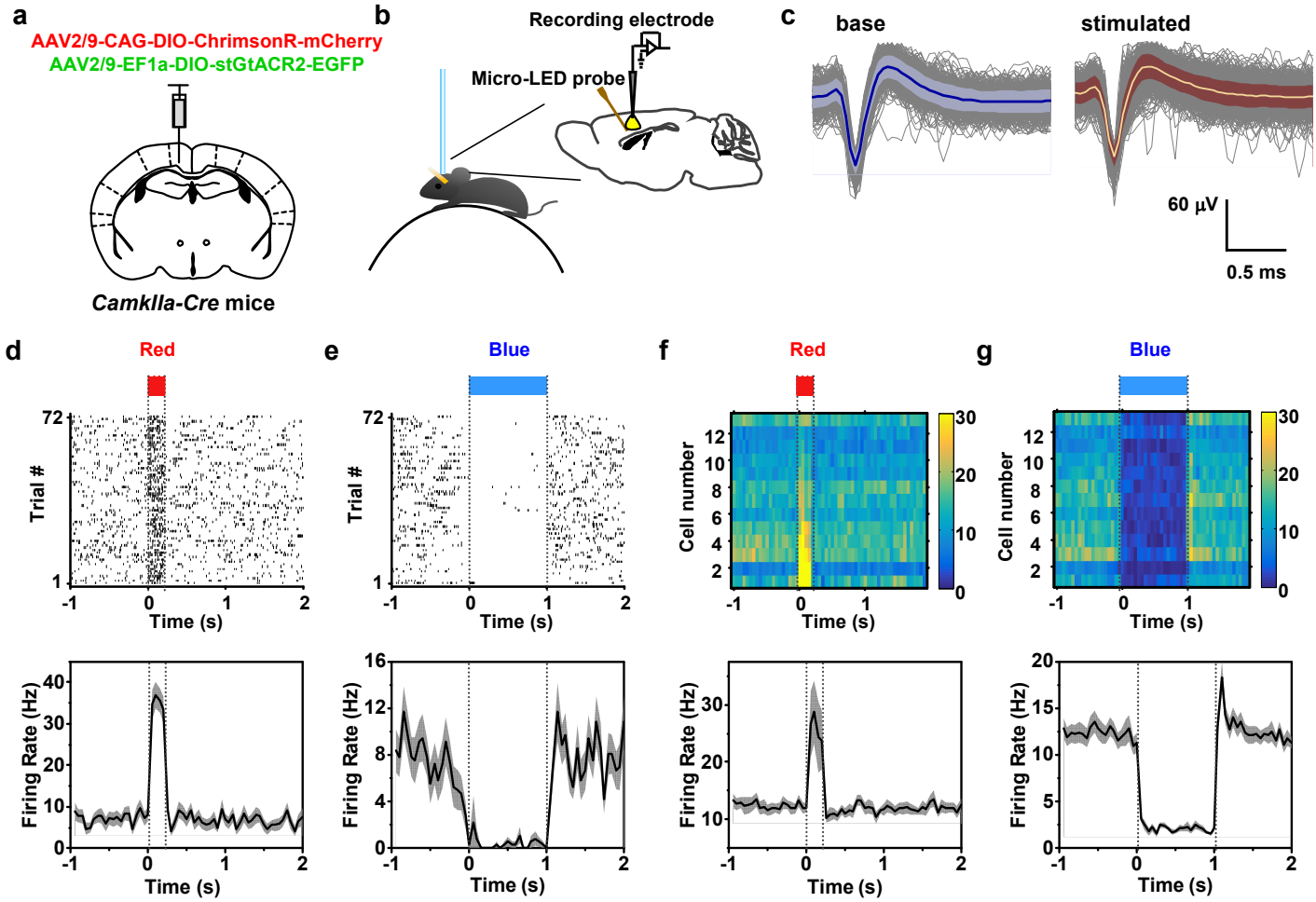

Figure 11. Bidirectional, *in vivo* optogenetic modulation of neural activities with dual-color illuminations in the cortex, combining with electrophysiological recordings. (a) Schematic strategy for co-expressing ChrimsonR and stGtACR2 in the primary somatosensory cortex of *CamkIIa-Cre* mice. (b) Illustration of the setup for simultaneous optogenetic stimulation and electrophysiological recordings by implanting the micro-LED probe and metal electrodes into the cortex of head-fixed mice. (c) Waveforms of a single unit recorded during baseline period before the red LED illumination (left) and during the red LED illumination period (right). Correlation coefficient between the two sets of waveforms is 0.9965. (d, e) Raster plots (top) and peri-stimulus time histogram (PSTH) plots (bottom) recorded for an example unit (n = 72 trials) for a sample unit during (d) red illumination (pulse width 0.2 s, LED current 10 mA) and (e) blue illumination (pulse width 1 s, LED current 1 mA). (f, g) Summarized results (top: heatmaps; bottom: PSTH plots) for multiple cells collected during (f) red illumination and (g) blue illumination (n = 13 cells from 2 mice, 50–100 trials for each cell).

Figure S12

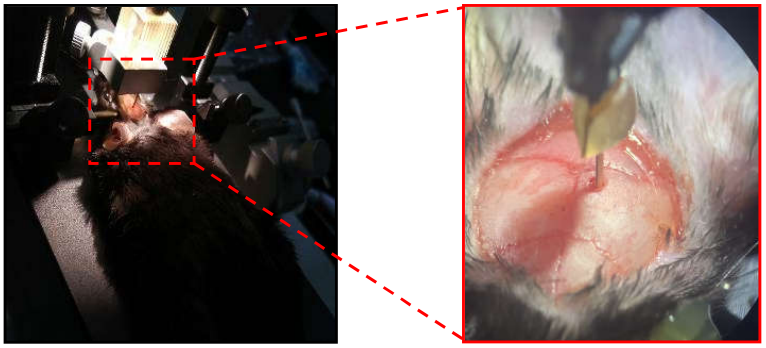

Figure S12. Photographs of the surgical procedure for probe implantation. A hole is created on the exposed skull of a mouse by drilling, and the dura is carefully removed by needle. The micro-LED probe is fixed on a holder controlled by a stereotaxic instrument, and slowly inserted into the targeted region.

Figure S13

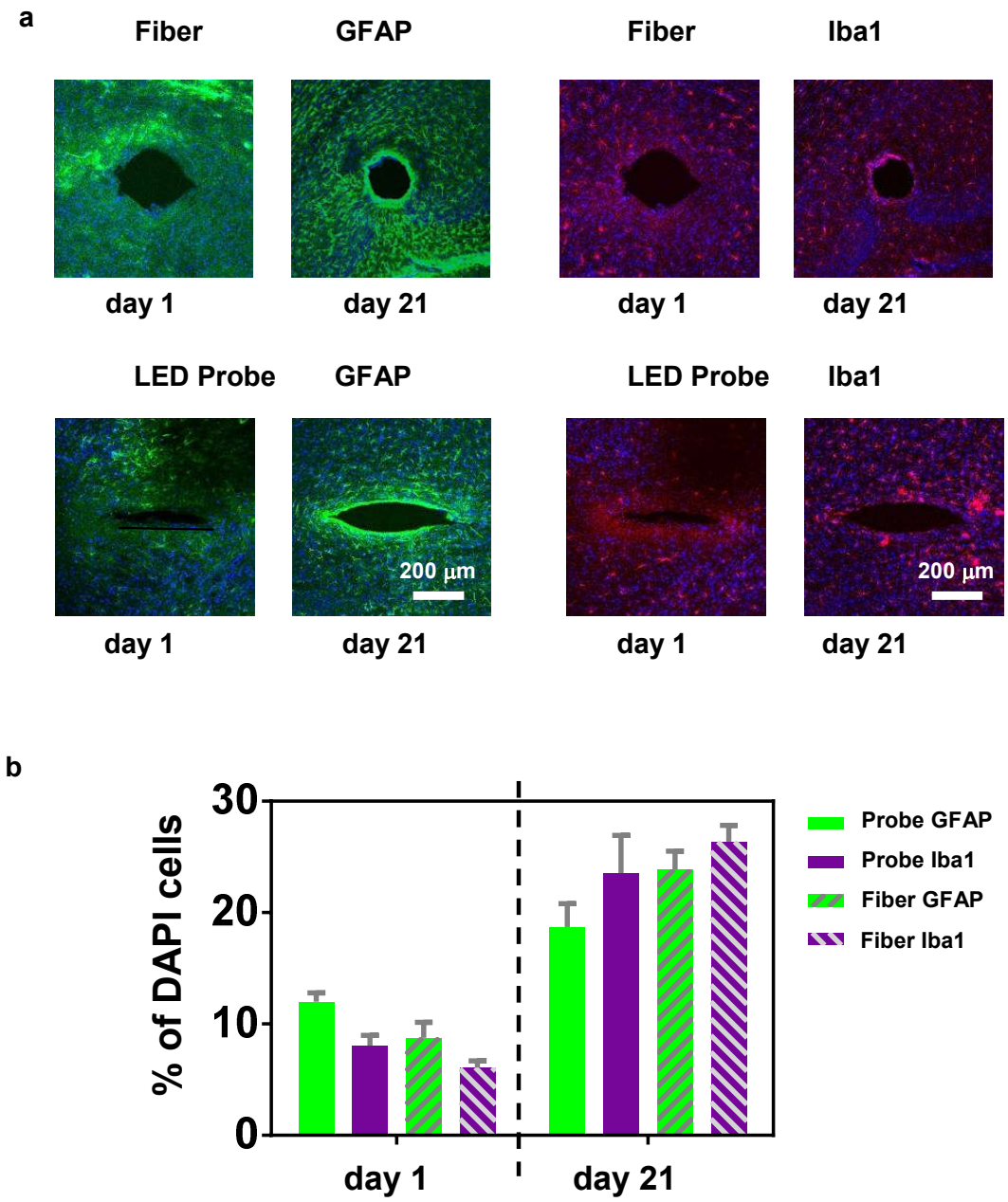

Figure S13. Immunoreactivity results showing the biocompatibility of the micro-LED probe, in comparison with those obtained with a silica based optical fiber. (a) Representative confocal fluorescence images of horizontal brain slices, showing immunohistochemical staining of astrocytes (GFAP) and activated microglia (Iba1) for both the LED probe and the fiber, after 1 day and 21 days implantation. Green: GFAP; Red: Iba1; Blue: DAPI. (b) Percentages of GFAP and Iba1 cell populations among DAPI cells collected at a distance of 200 µm from the edge of implantation. The LED probe and the fiber show similar results of inflammatory glial responses occurring after implantation. (n = 3 mice for each group).

Figure S14

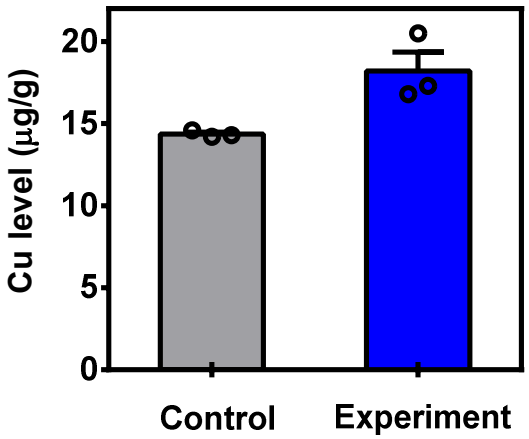

Figure S14. Measured Cu concentration in the brain tissue. The brain tissue is dried and analyzed with inductively coupled plasma mass spectrometry (Thermo ICP-MS iCAPQ, ThermoFisher, USA). The measured Cu level is 18.2 ± 2.3 μg/g for mice 5 weeks post probe implantation (experiment group). The result for the control group without probe is 14.4 ± 0.2 μg/g. The Cu levels in both cases are in the normal range (< 20 μg/g in mice brain, and 30–100 μg/g in human brain). n = 3 mice for each group.

References:

Chen Y, Wang L, Geng J-H, Zhang H-F, Guo L. Apolipoprotein E deletion has no effect on copper-induced oxidative stress in the mice brain. Biosci Rep 2018, 38(5).

Harrison WW, Netsky MG, Brown MD. Trace elements in human brain: Copper, zinc, iron, and magnesium. Clinica Chimica Acta 1968, 21(1): 55-60.

Figure S15

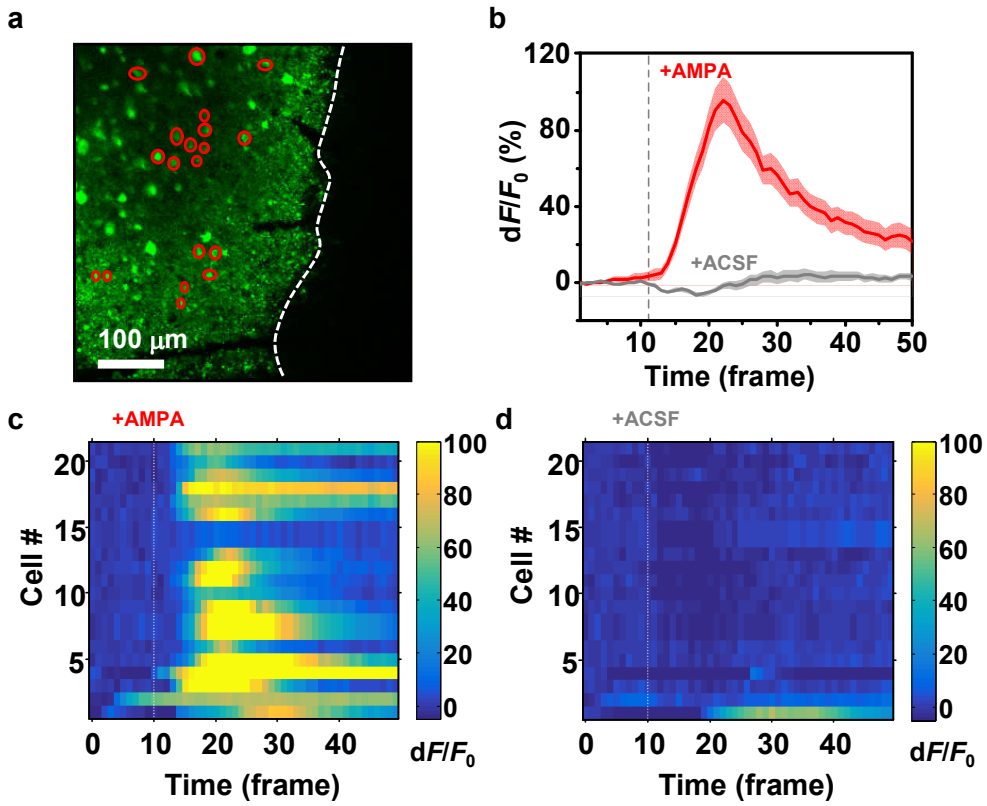

Figure S15. Imaging cellular calcium dynamics in acute brain slice. (a) Representative fluorescence image showing GCaMP6m-expressing cells near the probe region after 14 days implantation. Red circles mark active cells followed by AMPA administration. The dashed line marks the border of the lesion area. (b) Averaged calcium signal traces (dF/F_0) for all marked neurons after applying AMPA (red line) or pure ACSF (grey line) at frame 11, the sampling rate is 1.1 s / frame. (c, d) Heatmaps showing fluorescence variations in all 21 neurons after (c) applying AMPA or (d) pure ACSF.

Figure S16

a

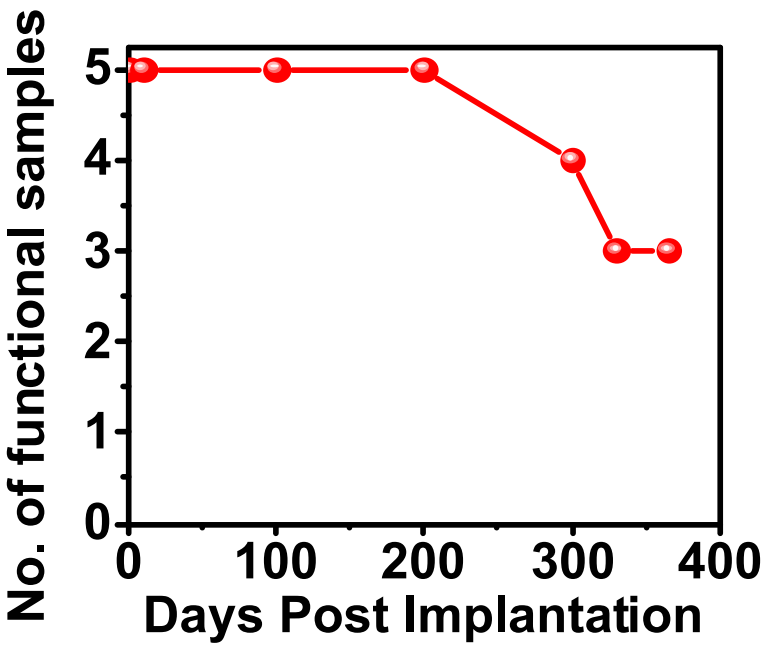

b

Mouse # / Date	Forward voltage (at current = 0.7 mA)	2019.09.05 (1 day)	2019.12.15 (100 days)	2020.03.25 (200 days)	2020.07.05 (300 days)	2020.08.05 (330 days)	2020.09.05 (365 days)
1	Red	1.81	1.82	1.81	1.83	1.83	1.83
	Blue	2.47	2.46	2.47	2.47	2.47	2.47
2	Red	1.83	1.83	1.83	1.83	1.85	1.85
	Blue	2.47	2.47	2.48	> 20 (broken)	-	-
3	Red	1.83	1.83	1.83	1.83	animal died	-
	Blue	2.47	2.47	2.47	2.47	animal died	-
4	Red	1.83	1.83	1.83	1.83	1.82	1.82
	Blue	2.47	2.47	2.47	2.47	2.46	2.46
5	Red	1.83	1.83	1.83	1.83	1.83	1.83
	Blue	2.46	2.46	2.47	2.46	2.46	2.46

Figure S16. (a) Chronic stability for the dual-color micro-LED probe. 5 probes are separately implanted into 5 behaving mice. Probes with both red and blue micro-LEDs operating in the normal condition are defined as "functional probes". (b) Summary of the performance for red and blue micro-LEDs in each probe. These probes are kept within the mouse brain. Their performance are evaluated by measuring LED's forward voltages at a constant current of 0.7 mA. After 365 days, the functional probes are taken out and still operate normally.

Figure S17

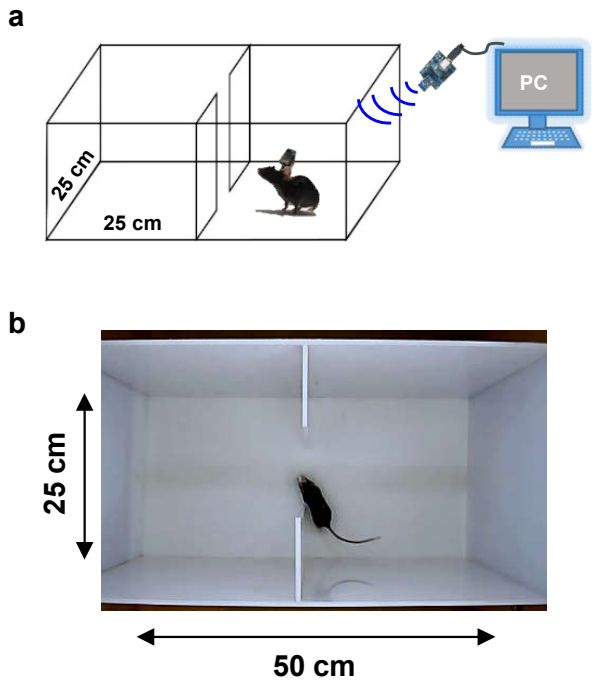

Figure S17. (a) Schematic diagram and (b) top-view photograph of the real-time place preference test with a two-compartment arena.

Figure S18

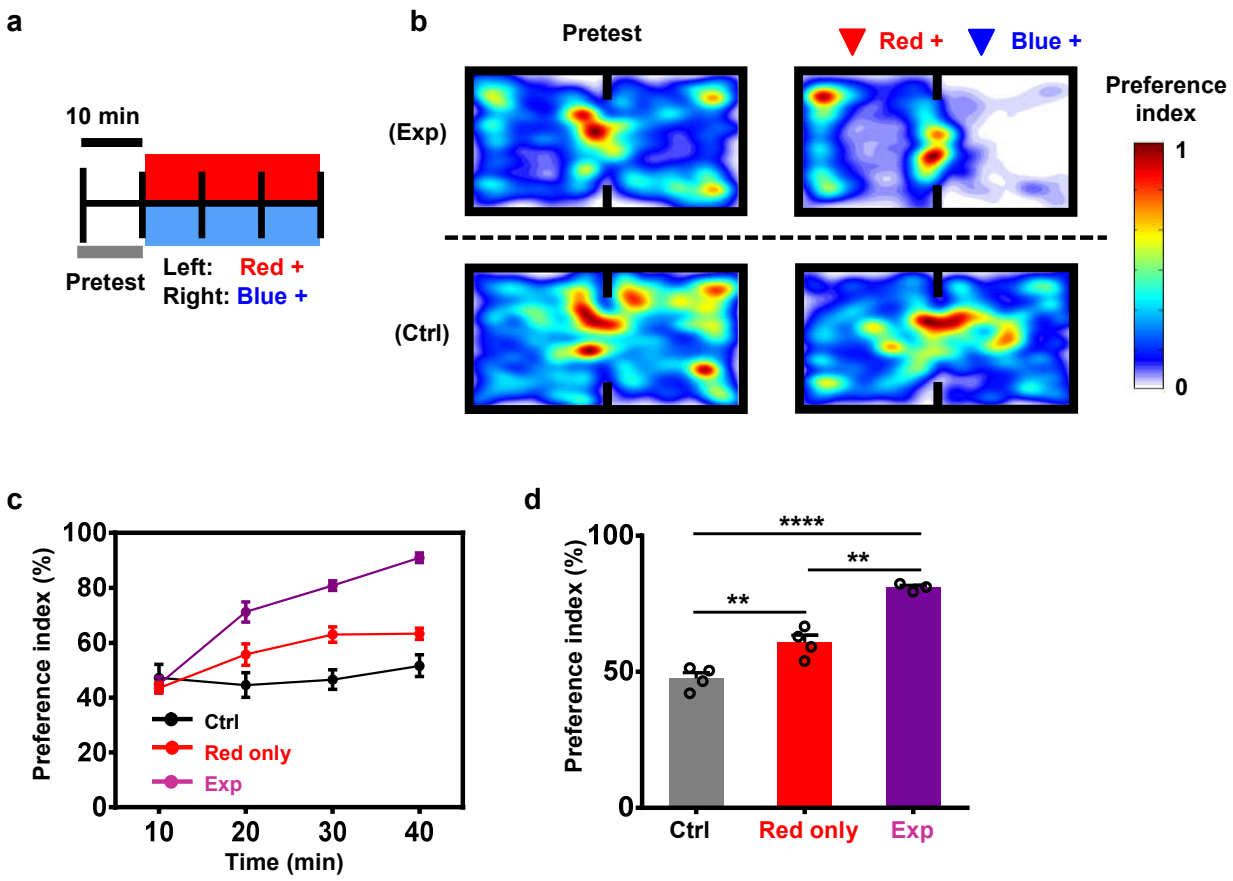

Figure S18. (a) Patterns used for optogenetic modulations, including a 10-min pretest, a 30-min red LED stimulation (20 Hz, 10-ms pulse, current 7 mA) in the left chamber and blue LED stimulation (continuous, current 5 mA) in the right chamber. (b) Representative heat maps comparing pretest and real-time preference behavior following both red (left chamber) and blue (right chamber) stimulation for mice expressing stGtACR2 + ChrimsonR (experiment group) and EGFP + mCherry (control group). (c) Preference indices measured at different times for mice under only red stimulations (red line, $n = 4$ mice), or red stimulations in the left chamber and blue stimulations in the right chamber (exp, purple line, $n = 3$ mice), and the control group with the red stimulation in the left chamber and blue light in the right chamber (ctrl, black line, $n = 4$ mice). (d) Summary of preference indices (the ratio of the time that mice spend in the left chamber to the whole recorded time) for mice under only red stimulations ($n = 4$ mice), or red stimulations in the left chamber and blue stimulations in the right chamber ($n = 3$ mice) for both experiment and control groups. Student's t test, ** $P < 0.01$, **** $P < 0.0001$.

Figure S19

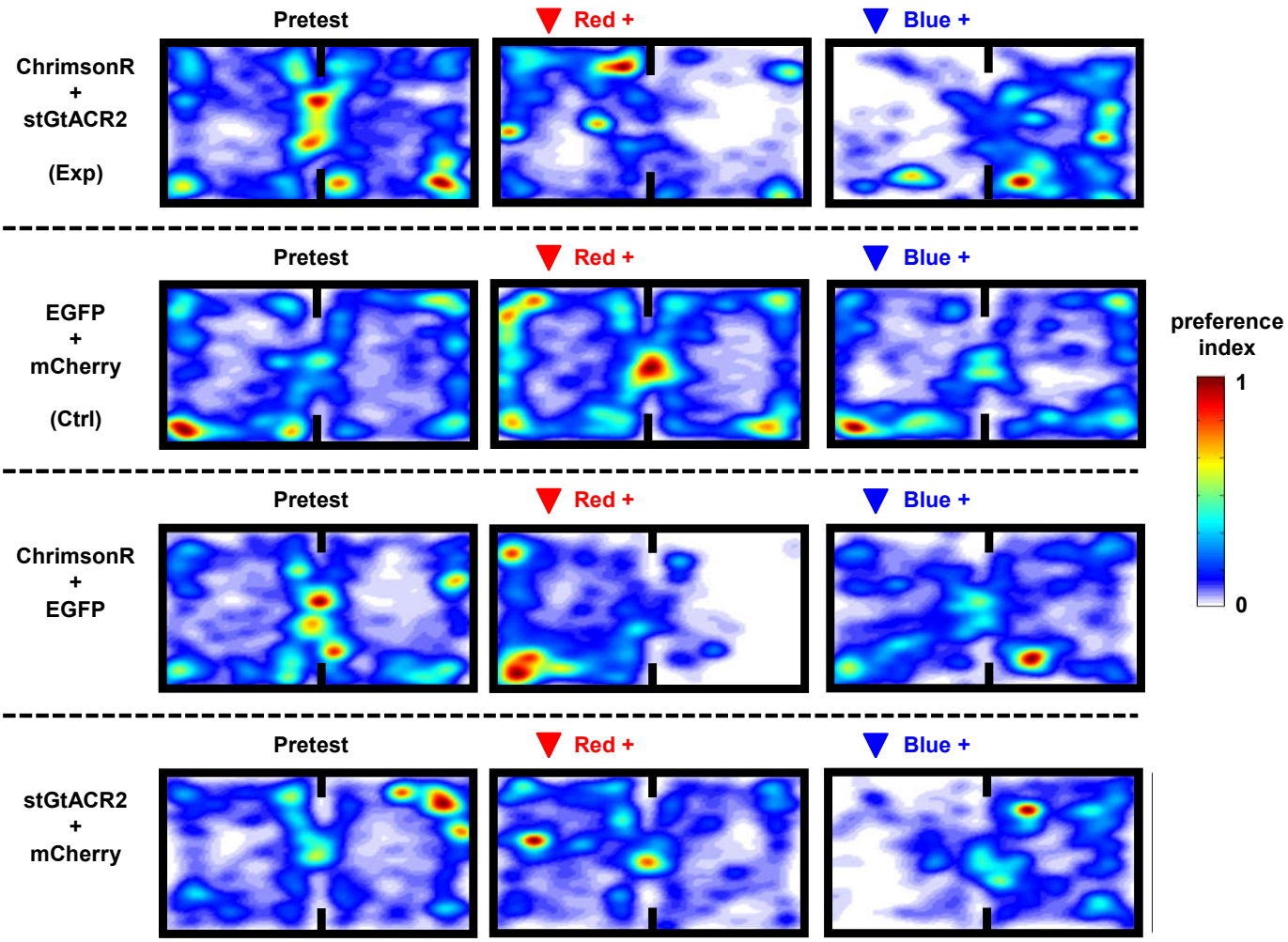

Figure S19. Representative heat maps showing real-time preference and aversion behavior following red or blue stimulation for mice expressing stGtACR2 + ChrimsonR (experiment, or Exp), EGFP + mCherry (control, or Ctrl), ChrimsonR + EGFP and stGtACR2 + mCherry. The data for ChrimsonR + stGtACR2 and EGFP + mCherry groups are identical to those presented in Fig. 3e.

Figure S20

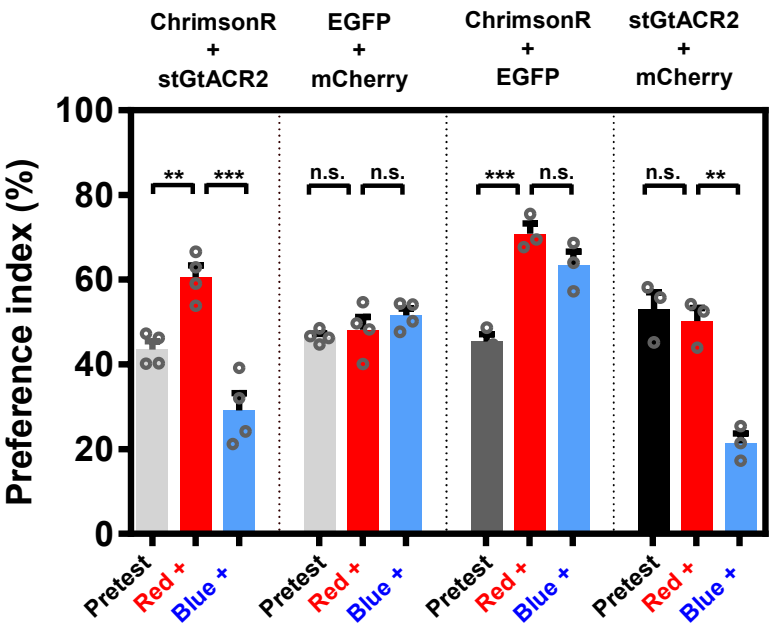

Figure S20. Summary of preference indices (the ratio of the time that mice spend in the left chamber to the whole recorded time) under red and blue stimulations for different mouse groups expressing ChrimsonR + stGtACR2 (n = 4 mice), EGFP + mCherry (n = 4 mice), ChrimsonR + EGFP (n = 3 mice), stGtACR2 + mCherry (n = 3 mice). Student's t test, ** $P < 0.01$, *** $P < 0.001$, n.s. $P > 0.05$. The data for ChrimsonR + stGtACR2 and EGFP + mCherry groups are identical to those presented in Fig. 3f.

Figure S21

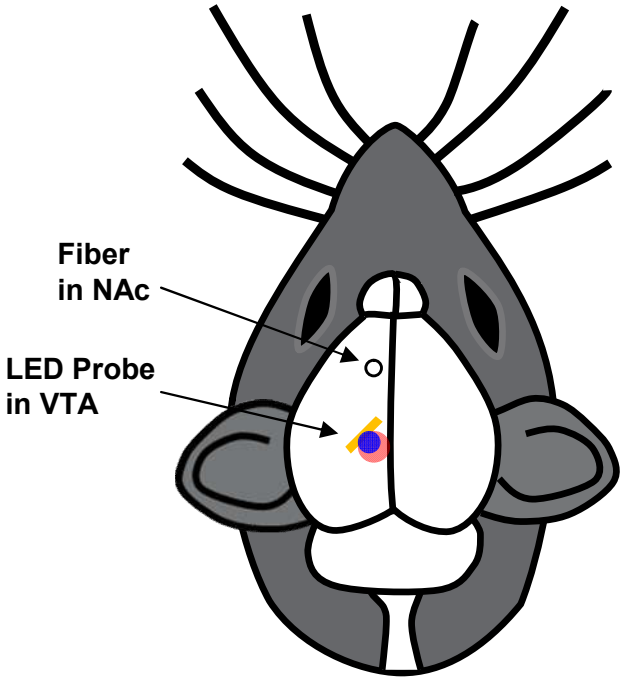

Figure S21. Schematic illustration (horizontal view) for the implantation of the fiber for DA recording in the NAc, and the dual-color LED probe for optogenetic stimulations in the VTA. The specific insertion angle is chosen for the LED probe, to minimize the optical crosstalk that disturbs the fiber photometric recording in the NAc.

Figure S22

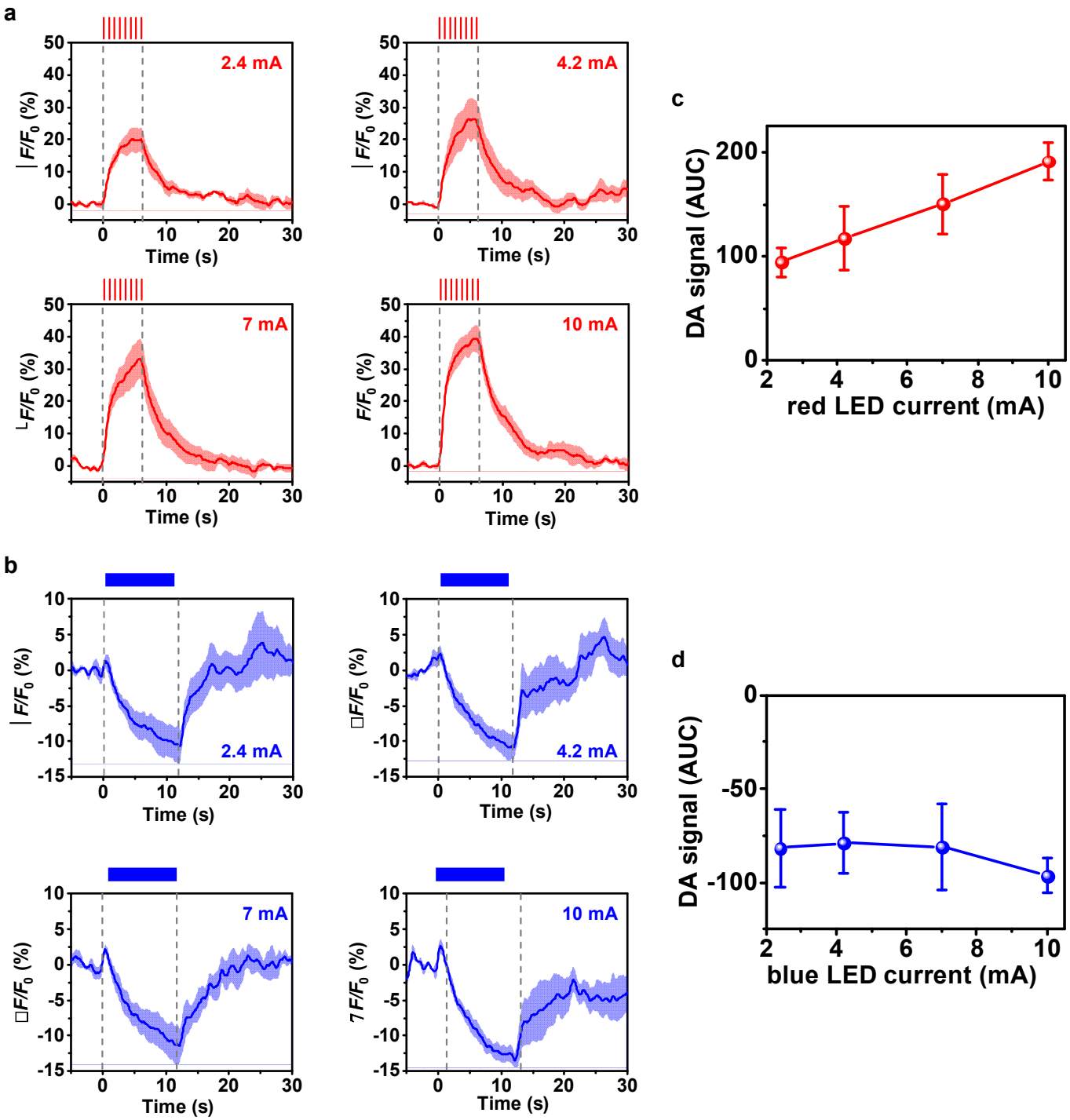

Figure S22. DA signals recorded as the fluorescence of $GRAB_{DA2m}$ in the NAc, in response to optogenetic stimulations applied in the VTA by red or blue micro-LEDs. (a, b) Representative traces of DA signals in response to stimulations by (a) the red LED (20 Hz, 20 ms, 6 s) and (b) the blue LED (continuous, 12 s) at various currents. The solid lines and shaded areas indicate the mean and s.e.m., respectively. (n = 4 mice). (c, d) Accumulative DA signals in response to (c) red and (d) blue stimulations under different LED currents. AUC: area under the curve during stimulation. The data for red LED at 7 mA and blue LED at 2.4 mA, and (c), (d) are identical to those presented in Figure 4c–4e.

Figure S23

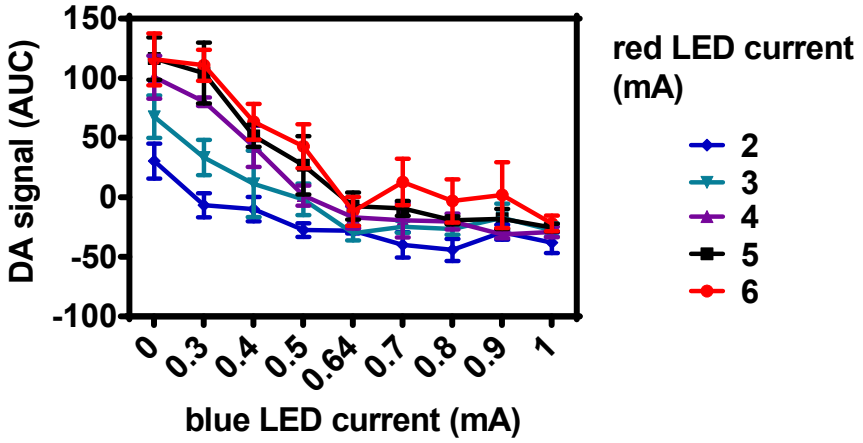

Figure S23. Detailed results of measured DA signals (AUC) with the combination of red and blue irradiance at different LED currents simultaneously for 6 s (n = 3 mice).

Figure S24

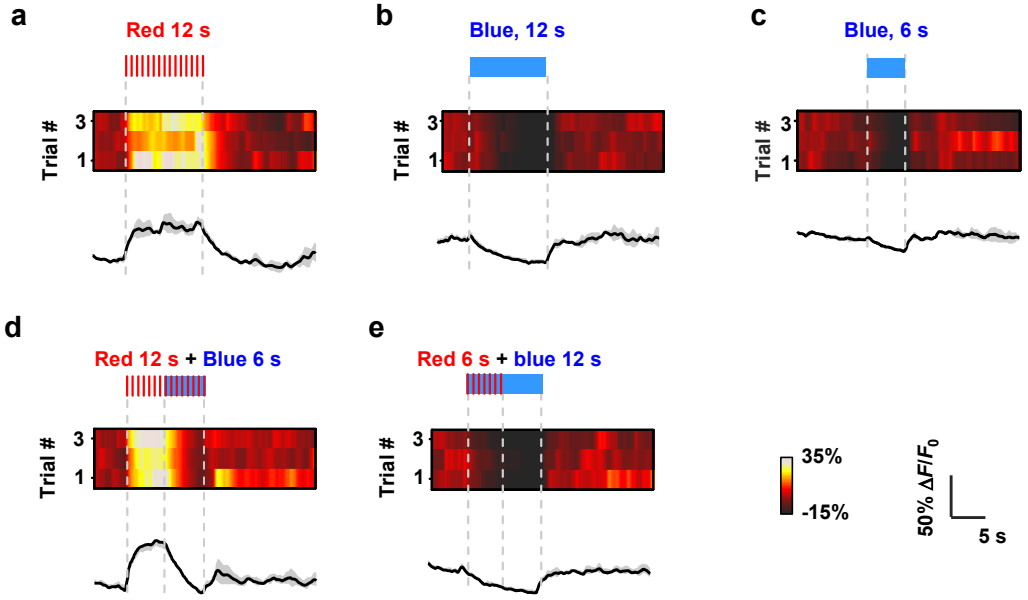

Figure S24. Example traces of optogenetically evoked DA transients for mice co-expressing stGtACR2 + ChrimsonR, in response to different stimulation patterns. (a) Red LED on, 20 Hz, 20-ms pulse, 10 mA, 0–12 s. (b) Blue LED on, continuous, 3 mA, 0–12 s. (c) Blue LED on, continuous, 3 mA, 6–12 s. (d) Red LED on 0–12 s and Blue LED on 6–12 s. (e) Red LED on 0–6 s and Blue LED on 0–12 s. The solid lines and shaded areas indicate the mean and s.e.m., respectively.

Movie S1

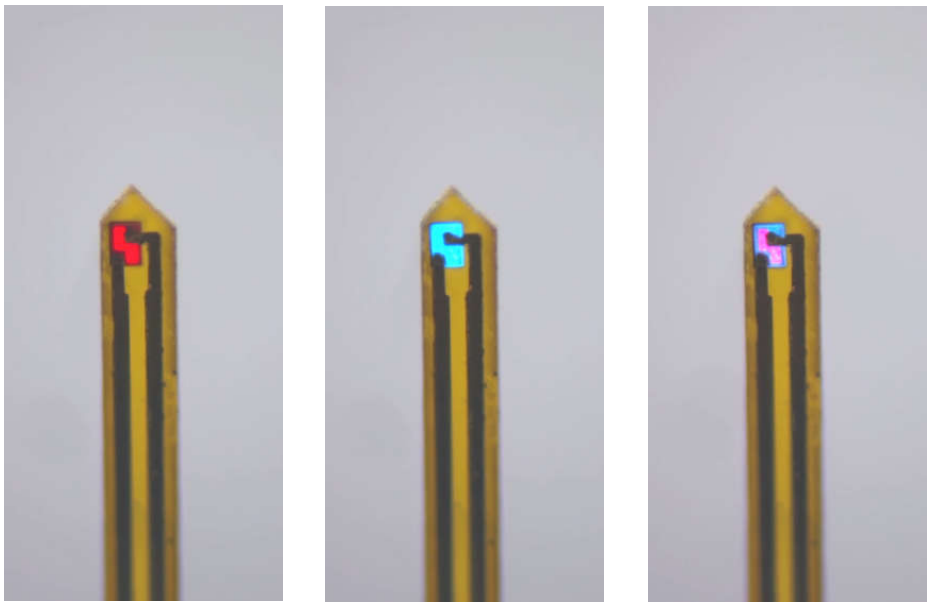

Movie S1. Video for dual-color micro-LED probe, displaying alternating blue and red emissions.

Movie S2

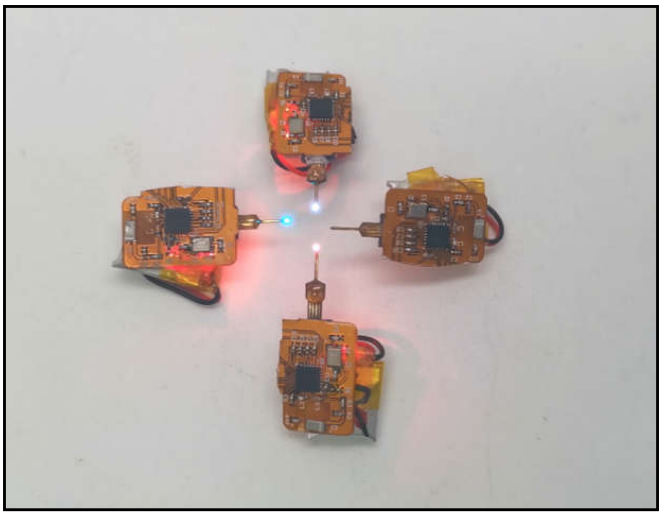

Movie S2. Video for multiple dual-color LED probes assembled with wirelessly operated circuit modules, showing capabilities for independent light emission control.

Movie S3

Movie S3. Video for four freely moving mice implanted with micro-LED probes and head-mounted circuits.

Movie S4

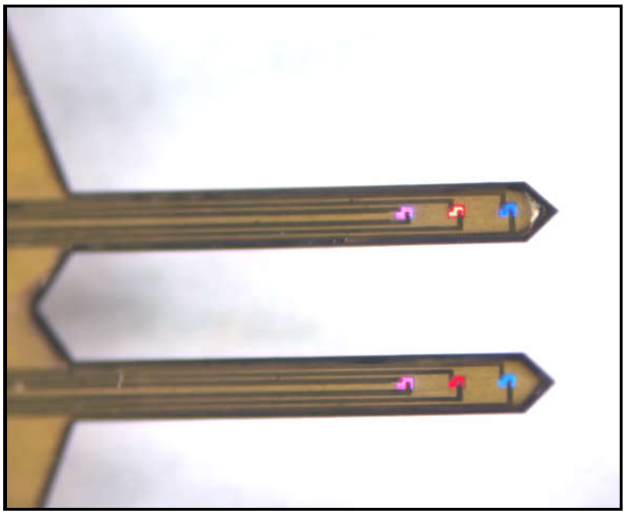

Movie S4. Video for multi-channel dual-color probes with 6 pairs of stacked red-blue micro-LEDs, displaying alternating blue and red emissions. These micro-LEDs are driven by a wired external power source.

Movie S5

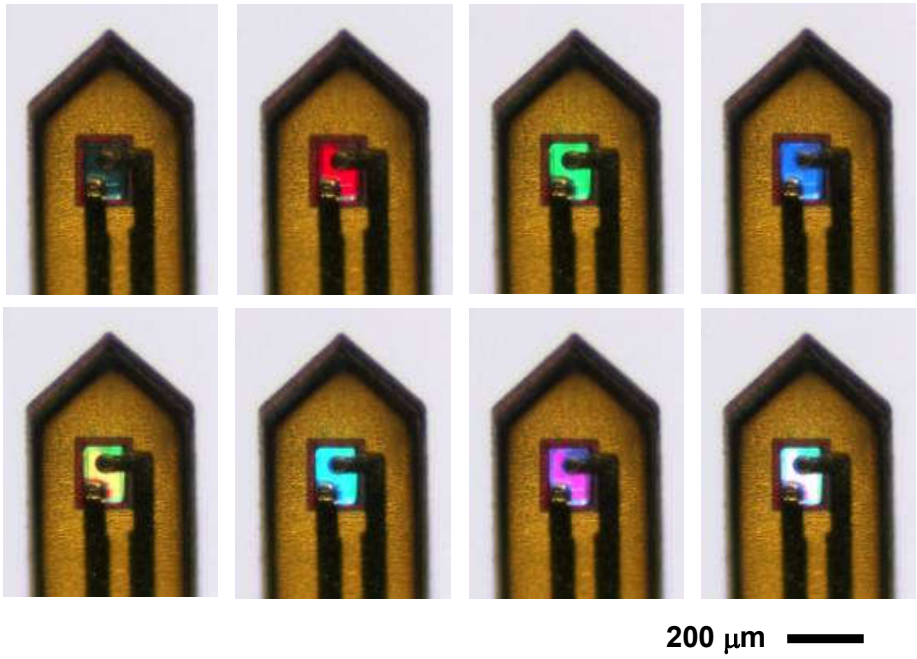

Movie S5. Video for a tri-color (red-green-blue) micro-LED needle structure, displaying different colors under current injection. These micro-LEDs are driven by a wired external power source.